# Nuclear Physics and Hadrontherapy

Daniel Cussol

*LPC Caen, ENSICAEN, Université de Caen Basse-Normandie, IN2P3/CNRS*

# ABSTRACT

The hadrontherapy uses light charged particles beams (mainly proton and $^{12}C$ ions) to irradiate tumors. These beams present a ballistic advantage with a maximum energy deposition at the end of the path (ie Bragg peak). A large dose can be delivered inside a deep tumor while the surrounding healthy tissues are preserved. Concerning the $^{12}C$ beams, an enhanced biological efficiency has been measured. Therefore there is an obvious advantage in using these beams. The nuclear fragmentation process of $^{12}C$ projectiles leads to deposit some dose beyond the Bragg peak and to spread the dose deposition around the beam direction. The basic knowledge of this process is of crucial importance to compute the dose deposition with an accuracy better than 3%. Additionally the fragments produced by this fragmentation process can be used for a real-time monitoring of the dose deposition in the patient.

In this lecture, we will define the quantities and the physical processes relevant for the hadrontherapy. The importance of the knowledge of the fragmentation process and its influence on the dose map will be presented and discussed. In the last part of this lecture, an overview of different instrumental developments (imaging, beam and dose monitoring) and different experimental measurements will be done.

## CONTENTS

Hadron therapy is an alternative way of treating cancerous tumors. It consists in irradiating tumors with protons (proton therapy) or light nuclei (alphas, carbon ions). Compared to conventional radiotherapy, it presents two main advantages: a precise ballistics, with a finite range and a maximum dose deposition at the end of the path of the ions (i.e. Bragg peak) and an enhanced biological efficiency in the Bragg peak region. This allows one to better target the tumor while preserving the surrounding healthy tissues. For carbon ions and heavier ions ($Z \geq 6$), another advantage is the increased biological efficiency: to obtain the same biological damages the dose needed for carbon ions is roughly one third of the dose delivered by X-rays. For protons and alpha particles, the dose needed is respectively 10% and 20% lower than the dose delivered by X-rays. The radio resistance due to the low oxygenation rate of cancerous cells (oxygen effect) almost vanishes when $Z \geq 6$ ions are used. Hence, light ion therapy may be an efficient means to treat radio-resistant tumors.

This lecture will show how nuclear physicists can contribute to improve and optimize hadron therapy. The first part will present the present status of hadron therapy and its mains advantages compared to the conventional X-ray therapy. The second part will present the main physical processes involved in the interaction between light ions projectiles and the matter. The influence of nuclear processes on the dose deposition will be shown in the third part. The last part of this lecture will list different application of nuclear physics for the computation and the monitoring of the dose deposition. A large part of this lecture has been inspired by the review paper of Dieter Shardt, Thilo Elsässer and Daniel Schulz-Ertner [Shardt10].

## I.   INTRODUCTION TO HADRON-THERAPY

### A.   Why hadron-therapy?

The cancer is the first cause of death in occidental countries. In France, around 300,000 new cases of cancers appear per year, one half of them being treated by X-rays therapy. The cure rate is around 45%. This success rate is obtained by using different therapeutic means: the surgery, the chemotherapy and the X-rays therapy. These therapeutic means are sometimes combined in order to increase the chance of success. Unfortunately, the treatment fails for 55% of the patients. The main reasons for these failures are the lack of local control on the tumor and the development of metastases. The goal of the radiation therapies is to destroy the cancerous tissues by using ionizing particles while preserving the surrounding healthy tissues.

The X-ray therapy is used since the seventies. The main drawback of this treatment means is the ballistics of the X-rays. As shown on figure 1, which shows the dose deposition induced by different projectiles with respect to the penetration depth in liquid water, the maximum of the deposition is located at a small penetration depth. Then the dose decreases slowly with respect to the penetration depth. It is difficult to accurately sight tumors deeply located in the body while preserving simultaneously the surrounding tissues. The original $^{60}Co$ sources ($\gamma$ rays of 1.17 MeV and 1.33 MeV) have been replaced by compact linear accelerators which deliver high energy X-rays. In these accelerators, electrons are accelerated and send to an conversion target. X-rays are produced by the bremsstrahlung process induced by the slowing down of the high energy electrons in the conversion target. In order to improve its efficiency, several irradiation procedures have been developed during the last decades: the Intensity Modulated Radio Therapy (IMRT), the Cyberknife and the tomotherapy. The IMRT uses multi-leaf collimators in order to conform the irradiation field to the external shape of the tumor. The Cyberknife is a very compact low energy accelerator mounted on a robot. This allows to use different beam incidences in 3D and hence concentrate the delivered dose on the tumor while spreading the dose on healthy

tissues. The tomotherapy is an extension of the IMRT which uses all possible incidences in a plane, the beam intensity depending on the beam incidence. These techniques are nowadays widely used all around the world and the therapists have now a good experience of X-rays therapies. The X-rays therapy is used as a reference to study the efficiency of other particle therapies.
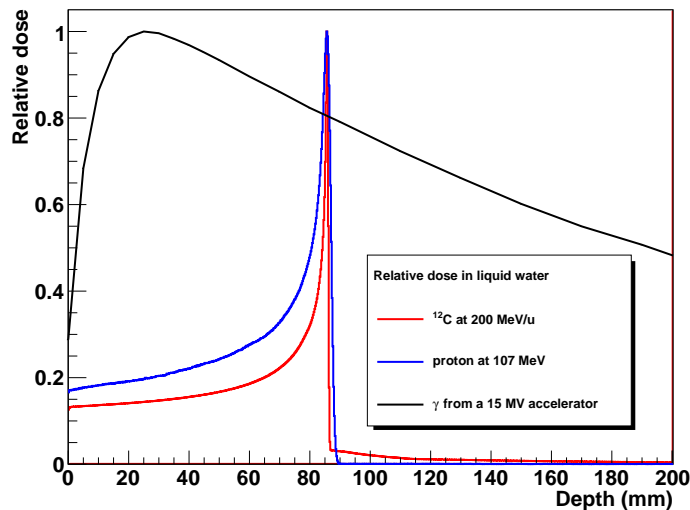


Figure 1. Evolution of the relative dose with respect to the penetration depth in water for different particles.

The charged particle beams have a better ballistics. The blue curve on figure 1 shows the dose deposition of a 107 MeV proton beam with respect to the penetration depth of the protons in liquid water. The red curve correspond to the dose deposition of a $^{12}C$ at 200 MeV/u. For both projectiles, it is clearly seen that the maximum deposition is located at the end of the path of the protons in a quite sharp peak. This peak is called the Bragg peak [Bragg05]. There is no dose deposition after this peak for protons and a weak dose deposition for carbons. The dose deposition before the Bragg peak is small (from 10% to 20% of the maximum). As it will be seen later, the location of the Bragg peak only depends on the particle incident energy. This allows to sight accurately the tumor with a weak dose deposition on the tissues located before the Bragg peak and with a very weak dose deposition after the Bragg peak. To paint the volume of a tumor, different beam energies are used. In that later case, the plateau resulting from the combination of different beam energies is called the Spread Out Bragg Peak (labeled SOBP). In that case, the dose deposition before the SOBP may be quite large (more than 50% of the maximum) depending on the size of the tumor and the number of beams used to paint it.

Another advantage of the particle therapies lies in the biological effects induced by the charged particles. To kill the same amount of cells lower doses are needed compared to X-rays (see [Shardt10] and references therein). This effect is parametrized by the Relative Biological Efficiency factor (labeled RBE). It is defined as the ratio of the dose $D_\gamma$ needed to kill a given amount of cells for X-rays to the dose $D_{part}$ needed to kill the same amount of cells for the particle under interest:

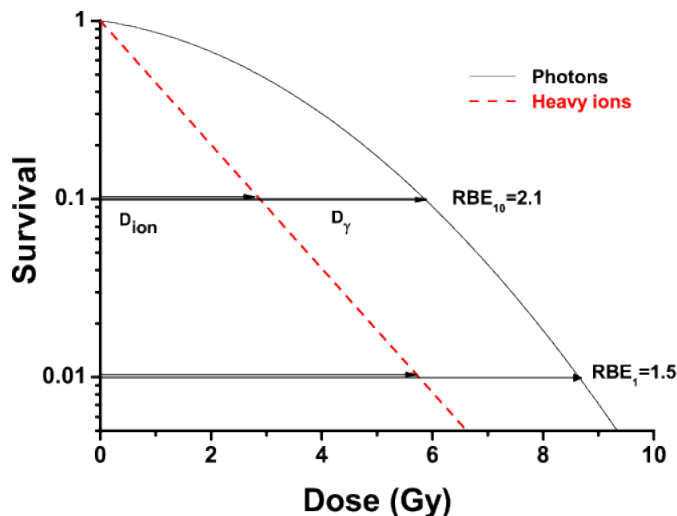$$RBE_{iso} = \frac{D_\gamma}{D_{part}} \qquad (1)$$

Figure 2. Survival curves and determination of RBE for cell inactivation for 10% and 1% survival level for a typical heavy ion irradiation. Extracted from [Shardt10].
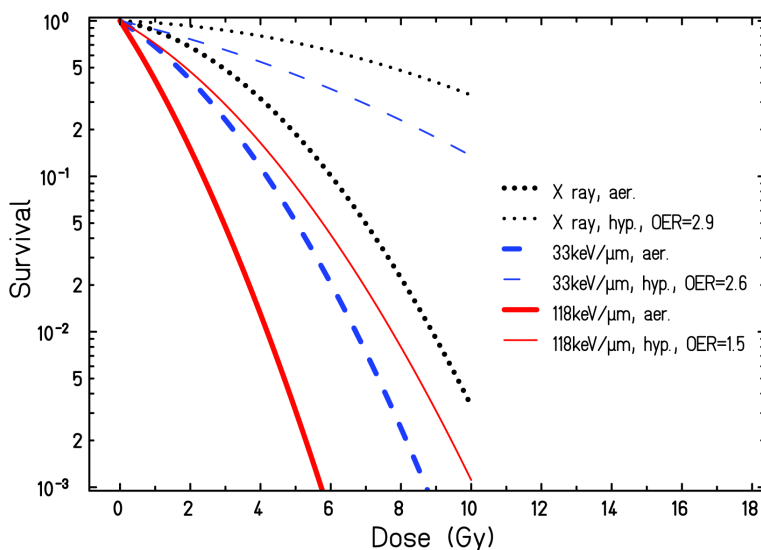


Figure 3. Influence of the oxygen level on cell survival of human kidney T-1 cells for carbon ions with different LET. Extracted from [Shardt10].

The figure 2 shows different survival curves (the rate of surviving cells with respect to the dose) for photons (full line) and for heavy ions (dashed line). It is seen that depending on the survival rate, the RBE can range from 1.5 to 2.1. The average RBE is around 1.1 for protons. The assumed RBE value for carbons is around 3.

Another biological effect is the so called "Oxygen effect": the cells with a low oxygenation rate (hypoxic cells) are more resistant to radiations than cells with a normal oxygenation rate (normoxic or aerobic cells). As a consequence, more dose is needed to destroy hypoxic cells (see [Shardt10] and references therein). Unfortunately, resistant hypoxic cells are located in the cancer tumours. This effect is parametrised by the Oxygen Enhancement Ratio (OER)
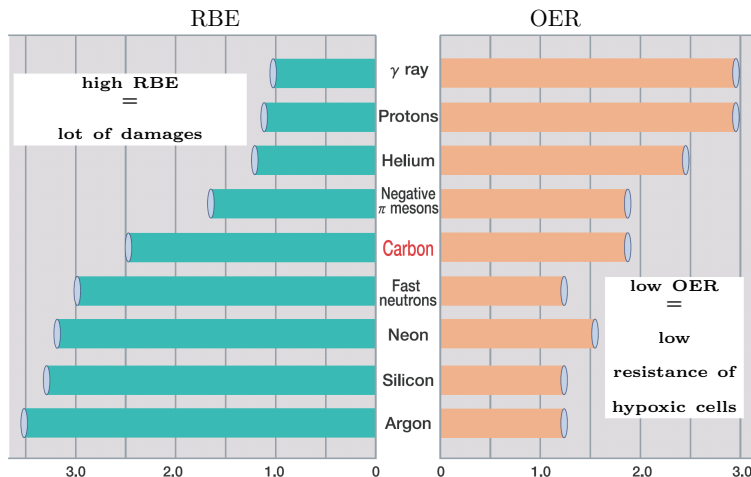
Figure 4. RBE (left) and OER (right) values of different particles.

which is defined as follows:

$$OER = \frac{D_{hypoxic}}{D_{aerobic}} \qquad (2)$$

where $D_{hypoxic}$ is the dose needed for heavy ions to kill a fixed amount of hypoxic cells and $D_{aerobic}$ is the dose needed to kill the same amount of aerobic cells. The figure 3 shows the survival curve for particles with different Linear Energy Transfer (LET) values for aerobic cells (full lines) and hypoxic cells (dashed lines). The OER value clearly depends on the LET value. For X-rays the OER value is around 3. For particles with low LET values like carbon ions at high energies, the OER value is around 2.6. For high LET values like carbon at low energies (close to the Bragg peak), the OER value decreases down to 2.

RBE and OER values are summarized on figure 4. One can see that the main improvement in using protons for radiation therapy is the ballistics of protons since the RBE value is only 1.1 and the OER value is close to the OER value of $\gamma$ rays. The RBE value increases with the size of the ion and the OER value decreases with the size of the ion. For ions heavier than neons the OER value is close to one: the "Oxygen Effect" has almost disappeared. A major improvement in radiation therapy may be achieved by using heavy ions: less dose is necessary to kill cancerous cells and no additional dose is needed to kill hypoxic radio-resistant cells. One can also notice that neutrons are also very efficient in killing cancerous cells. Unfortunately, neutrons have a very poor ballistics and an accurate sighting of a tumor is very difficult to achieve.

All these physical (ballistics) and biological (high RBE and low OER values) properties make heavy ions good candidates for their use in radiation therapy. They will be used for cancers with a low success rate with conventional therapeutic means. The main indications for charge particle therapy are radio-resistant and inoperable tumors like brain and head and neck tumors.

### B.   A short history of hadron-therapy

As soon as particle accelerators were available the charged particle therapy has been tested. R.R. Wilson is the first to suggest the use of proton beams for radiation therapy [Wil46]. The leading center is the Lawrence Berkeley National Laboratory where around 1,000 patients were treated from 1954 to 1974 with $\alpha$, $Ne$, $C$, $Si$, and $Ar$ beams. From

1975 to 1993 additional 1,000 patient were treated at the Massachusetts General Hospital with $Ne$ and $C$ beams only. These pioneering studies have lead to a collaboration between the LBNL and the Massachusetts General Hospital in order to develop the proton therapy in the USA. From 1961 to 2001 9,116 patients have been treated with proton beams. Since the nineties, almost 20 proton therapy centers have been build. The proton therapy is now widely spread in the USA. In may 2011, 73,800 patients have been treated with proton beams [PTCOG11a].

The carbon therapy has grown up only very recently. The leading country in the world is Japan where the first treatment center in Chiba was build in 1994. The HIMAC facility [Hir92] has treated around 5,500 patients with different pathologies. Two others centers are in duty in Hyogo and Gunma. In Europe, Germany is the leading country in carbon therapy. A first set of clinical trials has been done at the GSI in Darmstad. In between 1997 and 2007, 440 patient have been irradiated with carbon beams. In November 2009, the first European treatment centre has been opened at Heidelberg. Several project are on course in Italy, Austria and France. Since 1994, around 8,000 patients have been treated with carbon ions all around the world [PTCOG11a].

Nowadays, the hadron therapy is widely spread all around the world. Up to 36 hadron therapy centers are already in operation for both protons and carbon ions [PTCOG11b]. 24 projects are also on course, mainly in Japan, China, USA and European countries [PTCOG11c]. In France 2 complementary project are present: the ETOILE project which will be a treatment centre located in Lyon [ETOILE] and the ARCHADE project which will be dedicated to the research in hadron-therapy and located in Caen [ARCHADE].
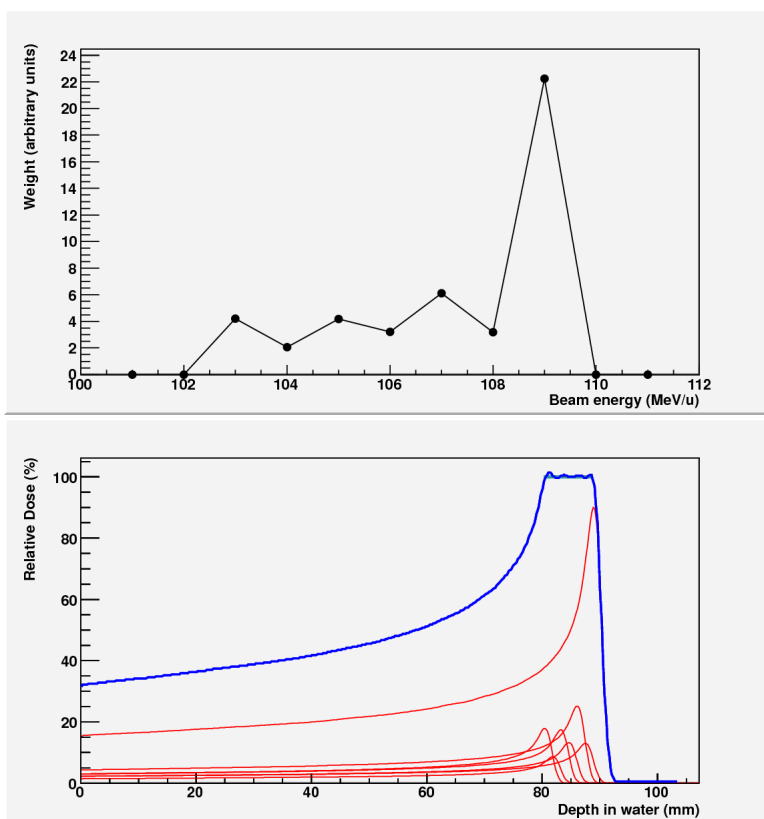


Figure 5. Energy weights distribution (upper panel) and corresponding SOBP (lower panel) for protons
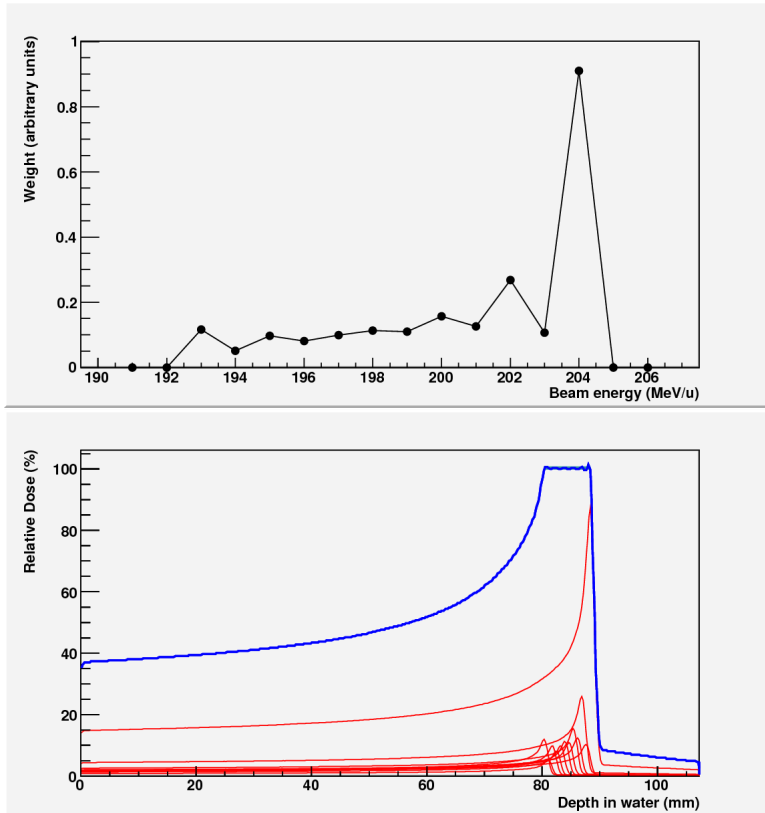
Figure 6. Energy weights distribution (upper panel) and corresponding SOBP (lower panel) for $^{12}C$ ions.

## C.    The Treatment Planning System

A Treatment Planning System (labeled TPS) is a software which computes the accelerator parameters in order to deliver a given 3D dose map for a given accelerator, a given patient and a given pathology. It includes the patient data (administrative data, clinical images), the graphical software for the organs identification and contouring and the contouring of the area to irradiate, and a dose computation module. At the Heidelberg Ion Therapy (HIT) facility, the TRiP software is used [TRiP]. It uses the Local Effect Model [LEM] to compute the biological effects (the cell survival rate) from the physical dose. This leads to an average value of the RBE around 3 at the Bragg Peak. The HIPLAN [Endo96] software is used at Japanese centers. A constant RBE value is assumed and taken as equal to 2. For protons, the RBE is often assumed to be constant with respect to the LET and equals to 1.1 [Paga02].

Here is a very simplified version of a TPS in one dimension. The purpose of this over-simplified example is to give a feeling of what a TPS is. Let assume one wants to irradiate a 1 cm long segment in water, its starting point (also called the proximal point by medical physicists) being at 8 cm. For that purpose, we have a set of physical depth-dose profiles (dose deposition with respect to the penetration depth) for protons and carbon beams. For a given incident energy $E_i$ the corresponding depth-dose profile is $D_i(x)$. For a set of beams with different energies, the dose at depth $x$ is given by: $D(x) = \sum_i N_i D_i(x)$. The biological dose is $D(x) = \sum_i N_i D_i(x) BF(x)$. The biological factor $BF(x)$ is equal to $RBE$ for aerobic cells or is equal to $\frac{RBE}{OER}$ for hypoxic cells. The goal is to find the values of $N_i$ to deposit a wanted biological dose $D_{wanted}(x)$ at depth $x$. One solution is to find the set of $N_i$ values which minimizes the following quantity:
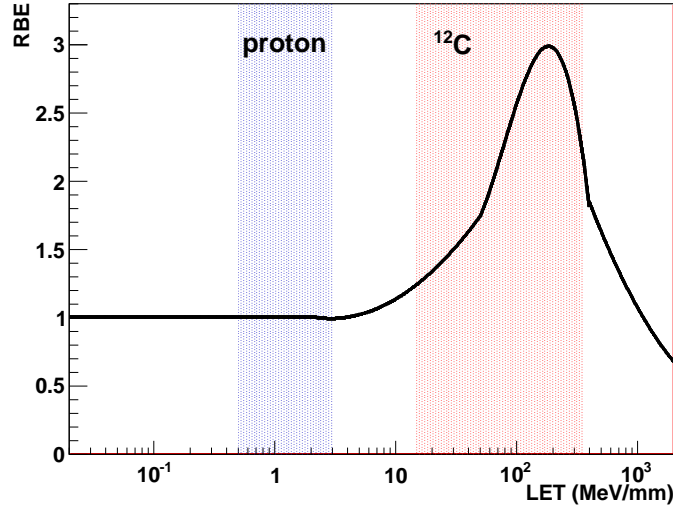
Figure 7. $RBE = f(LET)$ for the simplified biological model. The LET range for protons is indicated by the blue area. The red area corresponds to the $^{12}C$ LET range.

$$\chi^2 = \int (D_{wanted}(x) - \sum_i N_i D_i(x) BF(x))^2 dx \qquad (3)$$

This is equivalent to solve the following set of $n$ equations with the $n$ unknown $N_i$ values:

$$\frac{\partial \chi^2}{\partial N_i} = 0 \Rightarrow \int D(x)D_i(x)dx = \sum_j N_j \int D_j(x)D_i(x)dx \qquad (4)$$

The figure 5 shows the weights (the $N_i$ values) distributions for a set of dose profiles for protons (upper panel). The gap between two consecutive incident energies is 1 MeV. We see that the maximum weight corresponds to the maximum energy and hence the longest proton range needed to reach the farthest point of the segment. This range is called the distal range by medical physicists. The resulting physical deposition curve is shown on the lower panel of figure 5. The plateau in between 8 cm and 9 cm is called the Spread Out Bragg Peak (labeled SOBP). The small oscillations on the plateau are due to the discretization of incident energies. The weights distribution and the resulting SOBP for carbons are shown on figure 6. As for protons, the maximum weight corresponds to the energy for which the carbon's range is 9 cm.

In this example, the biological dose computation consists in affecting a biological factor to the physical dose. The RBE only will be used here. The following equation has to be solved:

$$\chi^2 = \int (D_{wanted}(x) - \sum_i N_i D_i(x) RBE_i(x))^2 dx \qquad (5)$$

which leads to the system of $n$ equation with the $n$ unknown $N_i$ values:

$$\frac{\partial \chi^2}{\partial N_i} = 0 \Rightarrow \int D(x)D_i(x)RBE_i(x)dx = \sum_j N_j \int D_j(x)RBE_j(x)D_i(x)RBE_i(x)dx \qquad (6)$$
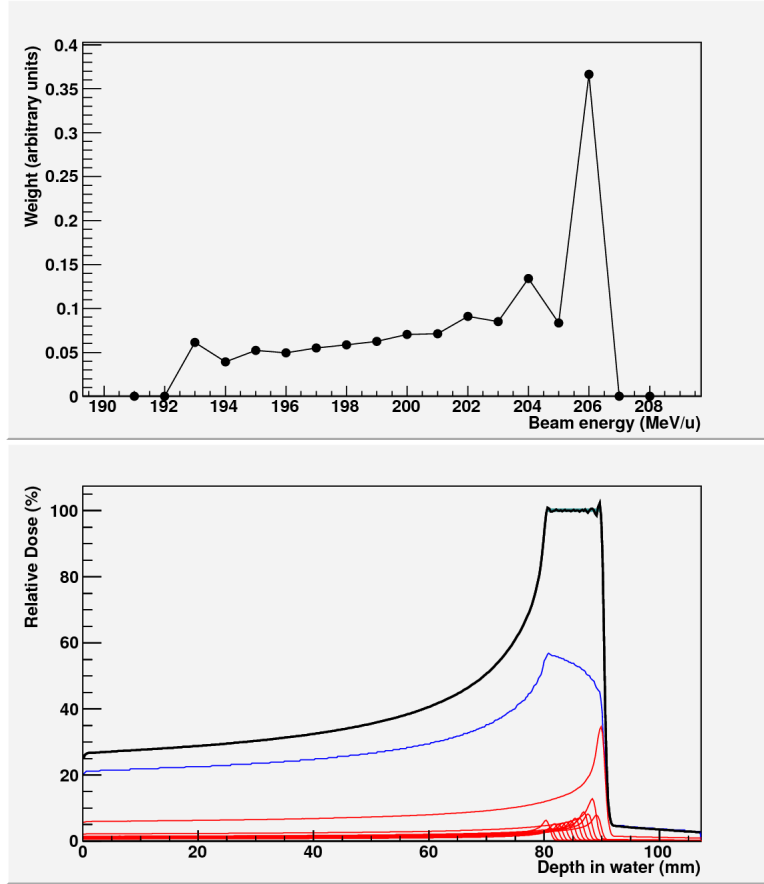
Figure 8. Energy weight distribution (upper panel) and corresponding biological SOBP (lower panel) for $^{12}C$ ions. The blue line corresponds to the physical dose and the black line corresponds to the biological dose.

In this simplified model, the RBE depends on the Linear Energy Transfer (labeled LET) of the particle only. As it will be seen later, the LET is close to the stopping power $\frac{dE}{dx}$ of the particle in the material on interest. The relationship between the RBE and the LET is displayed on figure 7. The typical LET values for protons ranges from 0.5 MeV/mm to 3 MeV/mm. In that case the RBE value is constant and equal to 1. Hence the biological dose will be equal to the physical dose. The resulting weights distribution and the SOBP are identical to the weights distribution and the SOBP obtained for the physical dose. For the carbon ions the LET values range from 20 MeV/mm to 250 MeV/mm. Hence the RBE values will vary in between 1.3 and 3 in the framework of this simplified model. The resulting weights distribution and SOBP are shown on figure 8. The effect of the biological model can be seen on both figures. The relative weight of the maximum energy is smaller than the maximum relative weight obtained for the physical SOBP. The physical dose (blue line on figure 8) is no more flat in between 8 cm and 9 cm. The use of another biological model would have lead to a different weights distribution and to a different physical SOBP. The knowledge of the biological effect is crucial if one wants to optimize the biological dose computation (see [Shardt10] and references therein).

Treatment Planning Software extend these basics concepts in order to deliver a 3D dose map. The figure 9 shows a result of the TPS TRiP in a clinical configuration for a carbon beam. The dose is deposited by using three different incidences. The area to irradiate if contoured by the black thick line in the head centre. The neighbouring organs at risk (optic
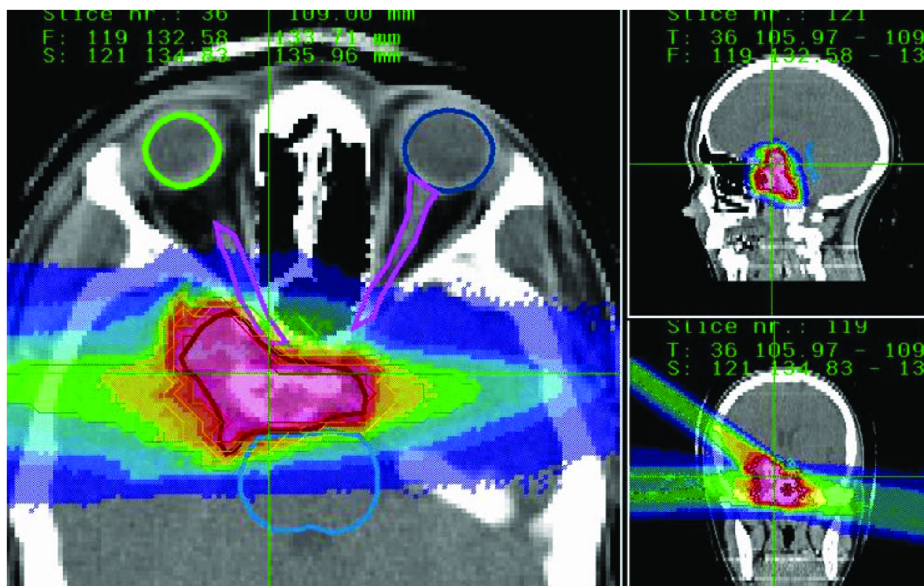
Figure 9. Biologically effective dose distribution optimized with the treatment planning system TRiP [TRiP] for a skull base tumor treated at GSI Darmstadt. With three fields an excellent sparing of critical organs (brain stem and optical nerves) is achieved. Extracted from [Shardt10].

nerves, eyes, spinal chord) are also contoured on this figure. The good ballistic properties of the carbon ions allows the clinicians to use incidences that graze the organs at risks.

## D.   Beam delivery

Once the weights distribution is known the machine parameters can be set. The particles have first to be accelerated. Two types of accelerators are used: the synchrotrons and the cyclotrons. Both types of accelerators are used in the proton therapy centres whereas synchrotrons only are used in carbon therapy centres. The advantage of synchrotron is that the beam energy can be easily changed from one bunch of particle to another. The main drawback is the huge size of such accelerators. For example, the synchrotron used at the HIT as a diameter of around 25 meters. The advantage of the cyclotron is its smaller size compared to synchrotron, especially for supra conducting cyclotrons. Medical cyclotrons have a fixed beam energy. The energy modulation is achieved by putting in the beam line pieces of matter of different widths. The drawback of this method is that secondary particles (mainly neutrons, protons and alpha particles) issued from nuclear interaction may pollute the beam. It also induces an energy spreading and a lateral spreading. An analysing magnet is necessary to remove as most as possible the polluting particles and to reduce the energy and the lateral spreading.

Since one wants to spare at most the healthy tissues surrounding the tumor, it is necessary to conform the dose map to the shape of the tumor. Two methods can be used: the passive beam delivery and the active beam delivery. The passive beam delivery consists in putting pieces of matter in the beam line in order to match at best the distal shape of the tumor, as shown on figure 10. The main advantage of this method is its simplicity. The total dose can be delivered without changing the accelerator parameters. Its main drawback is again the production of unwanted secondary particles, especially neutrons. This passive beam
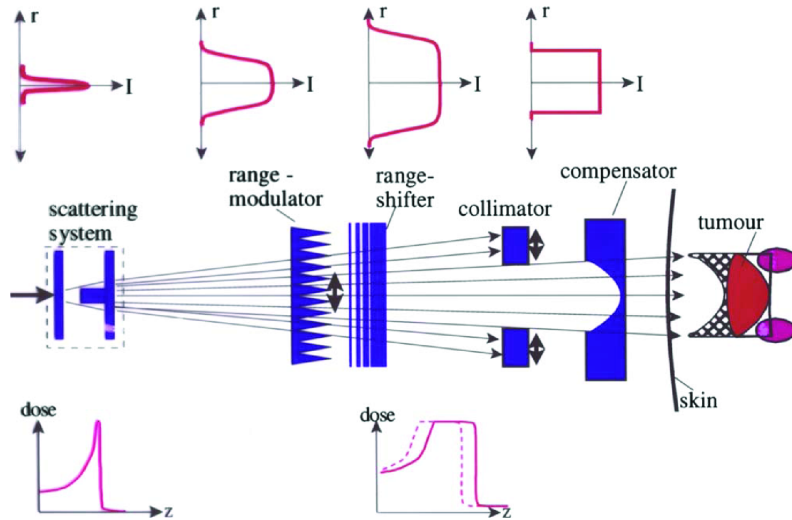
Figure 10. Sketch of a fully passive beam shaping system. The initially narrow beam is broadened by a scattering system and adapted to the target volume by various passive beam shaping devices. Adaption of the dose field to the distal contour of the target volume is achieved by a compensator, but results in unwanted normal-tissue dose in the proximal part (indicated by the doubly hatched area). Extracted from [Shardt10].

delivery is widely used in the treatment centers for both proton and carbon beams. In order to avoid the production of secondary particles, different active beam delivery methods have been developed. It consists in painting in 3 dimensions the tumor by deviating a pencil beam with magnets. The tumor is divided in planes, each of them corresponding to a given beam energy (see figure 11). It requires an excellent beam control and is hence very difficult to achieve. Such an active beam delivery has beam developed at the Paul Sherrer Institute in Switzerland for proton beams and at the GSI in Germany for carbon beams. This technique is operational at the HIT an at the proton therapy centre in Essen (Germany).

## II.  PHYSICS FOR HADRON-THERAPY

The use of charge particles for therapeutic purposes requires a very drastic dose control: the Bragg Peak location has to be known within 1 mm and the dose in the tumor has to be delivered within 3%. The two next sections will show what are the main physical inputs and the basics physical concepts which are necessary to compute the dose deposition and the range of charge particles in matter.

### A.  Elementary dosimetry

The definition of the absorbed dose $D$ in an elementary piece of matter of mass $dm$ can be found in the ICRU 51 report [ICRU51]:

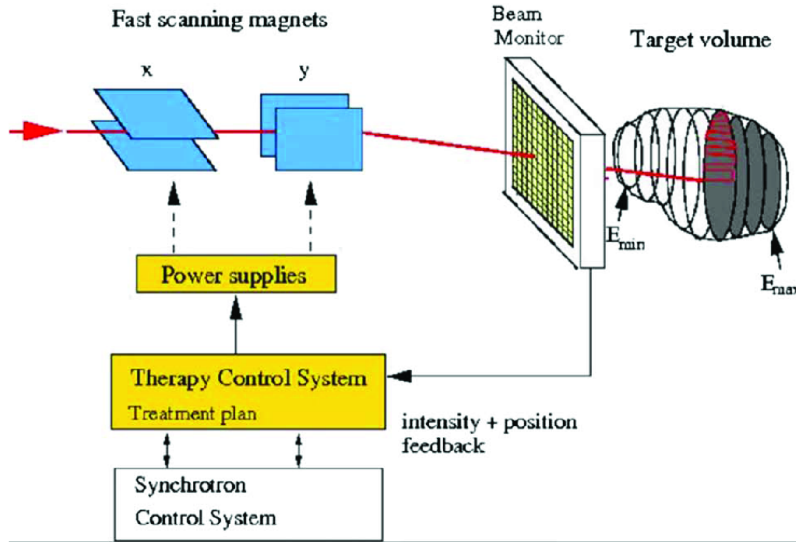$$D = \frac{d\bar{\epsilon}}{dm} \tag{7}$$

Figure 11. Principle of the intensity-controlled magnetic scanning system at GSI. The target volume is irradiated by moving a pencil-like ion beam (80–430 MeV/u $^{12}C$ ) with fast magnets over thin slices in depth. The required beam parameters are supplied on a pulse-to-pulse operation by the synchrotron (SIS) control system. Extracted from [Shardt10].

where $d\bar{\epsilon}$ is the mean amount of energy absorbed by in the elementary piece of matter. The dose unit is the Gray (labeled Gy). One Gray is equal to an absorbed energy of one Joule in one kilogram of matter. A more operational definition is used:

$$D = \frac{N}{dS} \frac{\left(\frac{dE}{dx}\right)}{\rho} \tag{8}$$

where $\frac{N}{dS}$ is the fluency of the beam and $\frac{dE}{dx}$ is the stopping power of the particle in the matter and $\rho$ the material's density. Since the fluency can be measured and the material's density is known, one only has to know the stopping power to compute the physical dose. All the physics lies in the computation the stopping power.

## B. Stopping power

In order to compute $\frac{dE}{dx}$, one has first to identify the physical processes which are responsible of the dose deposition and of the slowing down of particle in the matter. The main physical process involved is the inelastic collision of nuclei on the electrons of atoms present in the target matter. It is schematically shown on figure 12. In that process, the projectile of kinetic energy $E_c$ looses an energy $\delta E = e_c + I$ where $e_c$ is the energy of the out coming electron and $I$ the ionization potential of that electron. Most of the electrons are stopped in the vicinity of their emission point. Some of them have sufficient energy to deposit their energy far away the emission point (see figure 13). Hence, the energy $E_{dep}$ absorbed locally by the material is not strictly equal to the stopping power. The Linear Energy Transfer (labeled LET) which is the energy transfered by the material to the material per unit length is defined as follows:

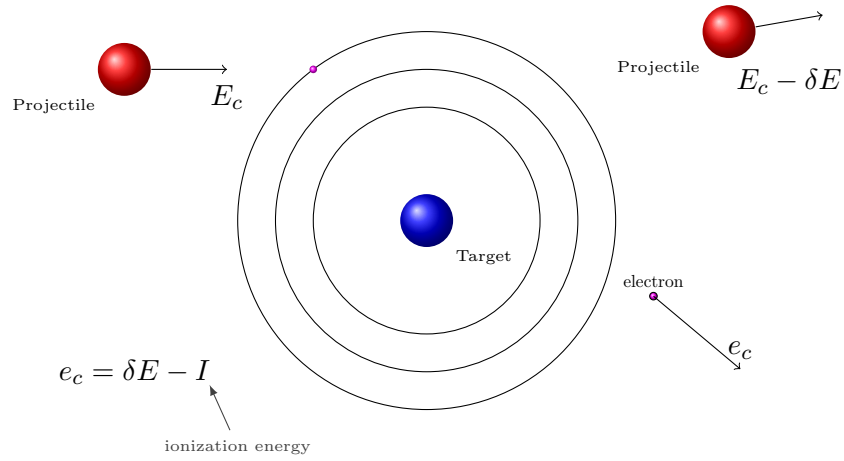$$LET = \left(\frac{dE}{dx}\right) - \sum Ec(e_\delta) \tag{9}$$
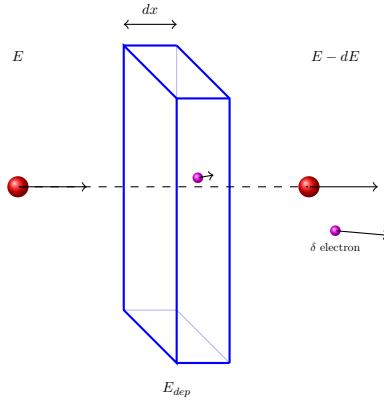
Figure 12. Inelastic collision of ions on electrons



Figure 13. Difference between LET and stopping power

where $\sum Ec(e_\delta)$ is the total kinetic energy of $\delta$ electrons which have an energy above a given threshold (typically the energy for which the range of electrons is greater than the unit length $dx$ under consideration). Some $\delta$ electrons are also coming from the previous elementary volume and will deposit their energy in the elementary volume in consideration. This roughly balances the energy of $\delta$ electrons produced in that volume. In a first approximation we can identify the Stopping Power, the LET and the absorbed energy in the elementary volume of thickness $dx$: $\left(\frac{dE}{dx}\right) \approx LET \approx \frac{E_{dep}}{dx}$.

As we have already seen for the computation of the RBE, the LET value for protons is around 3 MeV/mm at the Bragg Peak. To deposit 1 Gy at the Bragg Peak in water ($\rho = 1\,mg/mm^3$), the fluency value is given by:

$$1\,Gy = \frac{N}{dS}\frac{3\,10^6 \times 1.6\,10^{-19}}{10^{-6}} \implies \frac{N}{dS} \approx 2\,10^6 protons/mm^2 \tag{10}$$

For $^{12}C$ ions, the LET value is around 80 MeV/mm. The resulting fluency value is then:

$$1\,Gy = \frac{N}{dS}\frac{80\,10^6 \times 1.6\,10^{-19}}{10^{-6}} \implies \frac{N}{dS} \approx 8\,10^4\,^{12}C/mm^2 \tag{11}$$

### C.    The Bethe-Bloch formula

To compute the Stopping Power induced by many collisions on electrons, the Bethe-Bloch formula is used [Beth30, Bloch33a, Bloch33b]. A relativistic version of the Bethe-Bloch formula has been proposed by Fano [Fano63]:

$$\frac{dE}{dx} = \frac{4\pi e^4 Z_t Z_p^2}{m_e v^2}\left[ln\left(\frac{2m_e v^2}{<I>}\right) - ln(1-\beta^2) - \beta^2 - \frac{C}{Z_t} - \frac{\delta}{2}\right] \tag{12}$$

where $Z_t$ is the target atomic number, $Z_p$ is the projectile atomic number, $e$ the electron charge, $m_e$ the electron mass, $v$ the projectile velocity, $\beta = v/c$ where $c$ is the light velocity, $C$ is a shell correction factor, $\delta$ a density effect correction and $<I>$ the mean ionization energy. This last parameter is of crucial importance since it rules the energy loss of the projectile and its range. It can be estimated from the chemical formula of the material as follows:

$$ln(<I>) = \left(\sum_i \frac{\omega_i Z_i}{A_i}ln(I_i)\right) / \left(\sum_i \frac{\omega_i Z_i}{A_i}\right) \tag{13}$$

where

- $Z_i$ and $A_i$ : charge and mass numbers for element $i$

- $\omega_i$ : mass ratio of element $i$ in the material

- $I_i$ : ionization energy of element $i$ from Janni tables

It can be also determined from fits to experimental data. For liquid water, a value of $<I>= 79.7\,eV$ has been measured from energy loss measurements with 70 MeV protons [Bich92, Bich00]. Precision Bragg curve measurements for protons and various heavier ions have lead to values of $<I>$ ranging from 75 to 78 $eV$ [Kuma07, Paul07, Shardt08]. The $<I>$ value recommended by the ICRU is $<I>= 75\,eV$.

The influence of the $<I>$ value is shown on the figure 14. This figure displays the evolution of the location of the Bragg Peak with respect to the $<I>$ value for GEANT4 [GEANT4] and FLUKA [FLUKAa, FLUKAb] simulations. GEANT4 and FLUKA are Monte Carlo simulation frameworks which allows to follow the individual trajectories of ions in matter. In the GEANT4 simulation, it has been possible to select different ionization models (`emstandard_opt0`, `emstandard_opt1`, `emstandard_opt2`, `emstandard_opt3`) to described the inelastic collision of ions on electrons. We clearly see on that figure that the location of the Bragg Peak depends on:

- the ionization model

- the $<I>$ value

A variation of $\Delta <I>= 5\,eV$ on the $<I>$ value leads to a variation of around 1 $mm$ on the range. Since the accuracy on the range required by the hadron therapy is 1 $mm$, the $<I>$ values have to be known within $\approx 5\,eV$ for a given ionization model.
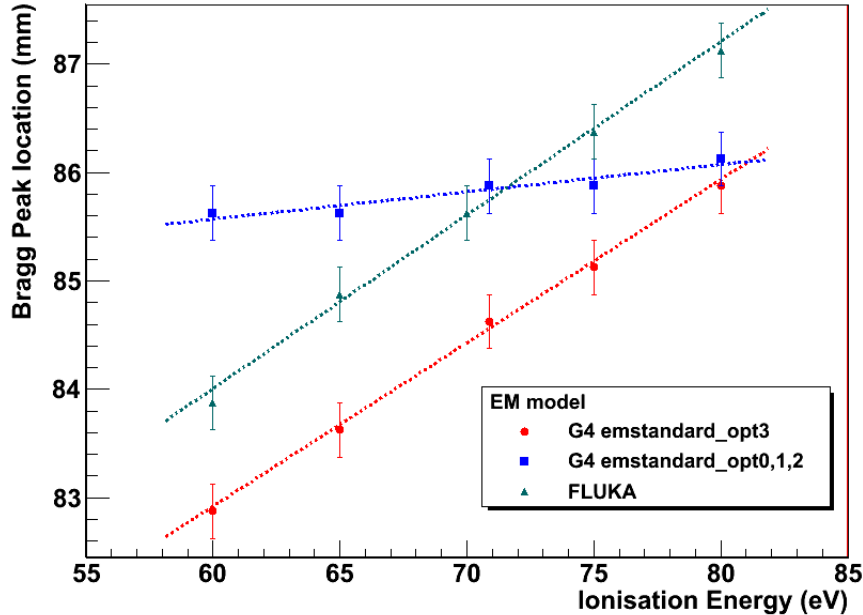
Figure 14. Variations of the Bragg Peak location with the mean Ionisation energy obtained for GEANT4 and FLUKA simulations.

## D. Other physical processes

Several other physical processes are involved in the slowing down of charged particles in matter. The elastic Coulomb scattering lead to trajectories that are not a straight lines. It induces a range and a lateral spreading. The elastic collisions with target nuclei become important at low energies $E_c < 10keV/u$, i.e. for the few last micrometers of the projectile path. This process is neglected for hadron-therapy applications. The electron capture lead to change the effective charge of the projectile [Bark63]. In the Bethe-Bloch equation the $Z_p$ value has to be replaced by $Z_{eff} = Z_p \left[ 1 - exp(-125\beta Z_p^{-2/3}) \right]$. This process is important at $E_c < 10MeV/u$ (close to the Bragg Peak). The Bremsstrahlung process is neglected for hadron-therapy applications. The last but not least process is the nucleus-nucleus collisions which produces secondary particles with longer ranges than the projectile's range. The influence of this process on the dose map will be seen in details in the next section.

The figure 15 shows the stopping powers of protons and $^{12}C$ ions with respect to the kinetic energy of the projectile. For protons, the inelastic collision on electrons is the dominant process for all energies. For $^{12}C$ ions, this process is also dominant except for the last few micrometers of path.

## E. Particle range and particle energy

The figure 16 shows the range of different particle type with respect to their incident energies. These curves have been obtained for the liquid water using the SRIM [SRIM] simulation. For a given energy per nucleon (or a given velocity), the range of a projectile is proportional to the ratio $\frac{A}{Z^2}$ where $A$ is the projectile number of mass and $Z$ the projectile
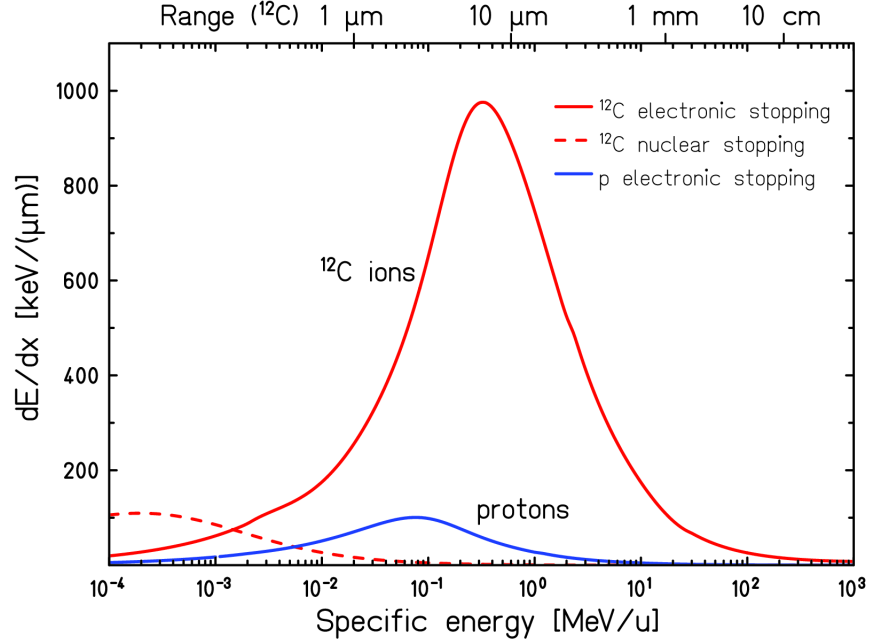
Figure 15. Specific energy loss $dE/dx$ of $^{12}C$ ions and protons in water. The range of $^{12}C$ ions in water corresponding to their specific energy is indicated at the top. Extracted from [Shardt10].

number of charges.

For the hadron-therapy applications, it is needed that the projectile reaches the deepest tumor in a human body. This lead to a maximum range of around 30 cm in liquid water (see 17). The corresponding energy range for protons is then from 0 to 220 MeV and from 0 to 425 MeV/u for $^{12}C$ ions.

## F. Range and angular stragglings

The random character of the inelastic collisions lead to an energy straggling which can be parametrized the following way [Vasil57, Bohr40, Ahlen80]:

$$f(\Delta E) = \frac{1}{\sqrt{2\pi}\sigma} exp \frac{\left(\Delta E - \overline{\Delta E}\right)^2}{2\sigma_E^2} \qquad (14)$$

where $\sigma_E$ has the following expression:

$$\sigma_E = 4\pi \, Z_{eff} \, Z_t e^2 N \Delta x \left[\frac{1 - \beta^2/2}{1 - \beta^2}\right] \qquad (15)$$

where $Z_t$ is the target number of charges, $Z_{eff}$ is the projectile effective charge and $\beta$ the projectile velocity in $c$ units and $E$ the projectile kinetic energy.

The resulting range spreading is related to the energy straggling $\sigma_E$:

$$\sigma_R^2 = \int_0^{E_i} \left(\frac{d\sigma}{dx}\right) \left(\frac{dE}{dx}\right)^{-3} dE \qquad (16)$$
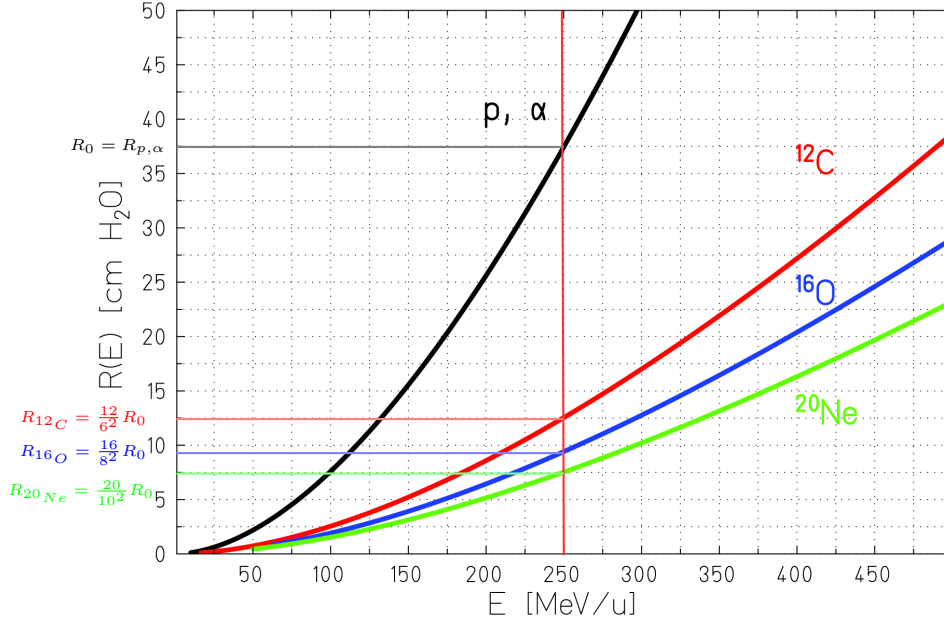
Figure 16. Range of different types of particles in liquid water computed with the SRIM simulations.

The relative range straggling can then be expressed this way:

$$\frac{\sigma_R}{R} = \frac{1}{\sqrt{M}} f\left(\frac{E}{Mc^2}\right) \tag{17}$$

where $M$ is the projectile mass and $f$ is a slowly varying function depending on the absorber [Rossi52]. As a consequence, the relative range straggling is smaller for heavier particles; This is shown on figure 18 which displays the Bragg Curve for protons and $^{12}C$ ions having the same range in water [Shardt08]. Due to the $1/\sqrt{M}$ factor, the range straggling of $^{12}C$ ions is smaller than the range straggling of protons by a factor of $\approx 3.5$.

The lateral spreading of the beam is also smaller for the heavy ions than the lateral spreading of protons. This is a big advantage when the cancerous tumor is located close to Organs At Risk (OAR). The lateral spreading is mainly due to the multiple Coulomb scattering process. For small deflections, the angular distribution of the projectile after passing through a distance $d$ of absorber can be described by a Gaussian distribution [High75, High79]:

$$F(\vartheta, d) = \frac{1}{\sqrt{2\pi}\sigma_\vartheta} exp\left(-\frac{\vartheta^2}{2\sigma_\vartheta^2}\right) \tag{18}$$

where

$$\sigma_\vartheta[rad] = \frac{14.1 MeV}{\beta pc} Z_p \sqrt{\frac{d}{L_{rad}}} \left[1 + \frac{1}{9} log_{10}\left(\frac{d}{L_{rad}}\right)\right] \tag{19}$$

with $L_{rad}$ the radiation length parameter of the absorber material. Values of $L_{rad}$ for common materials can be found in [Tsai74] and can be easily computed for compounds (e.g., $L_{rad} = 36.08$ for liquid water). The variations of the lateral spreading with respect to the penetration depth in liquid water is shown on figure 19 for different projectiles. These curves have been
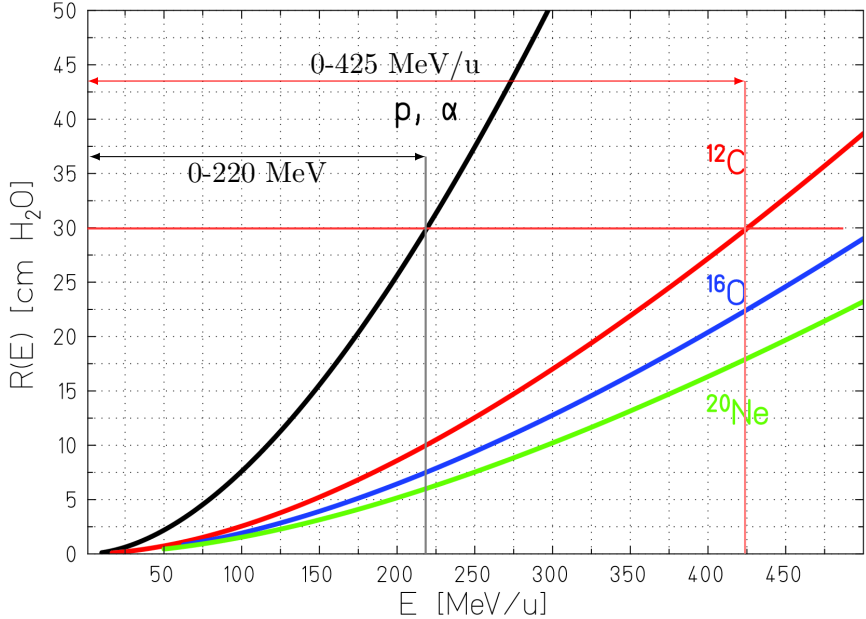
Figure 17. Energy domain of interest for hadron therapy according to SRIM simulations.
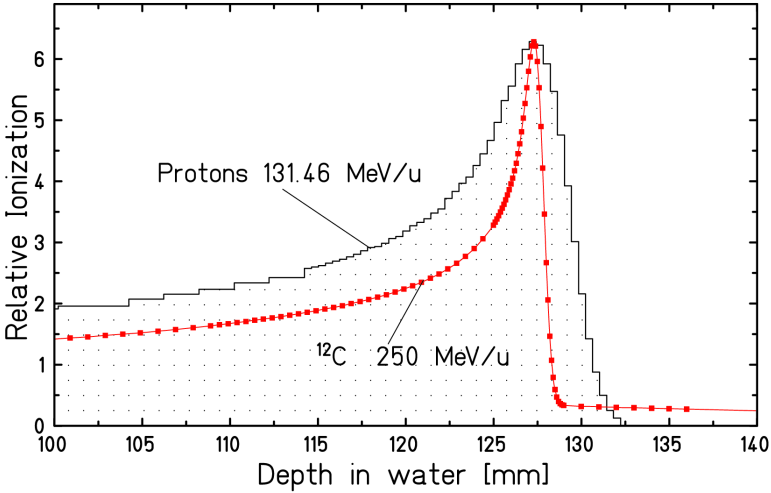


Figure 18. Measured Bragg peaks of protons and $^{12}C$ ions having the same mean range in water. Extracted from [Shardt10].

obtained with SRIM. As already mentioned, the lateral spreading at the same penetration depth decreases when the mass of the projectile increases.

## G. Summary

This part has shown that the ballistic properties of charged particles can be used to sight accurately cancerous tumors in the human body. The energy straggling and and the lateral

Figure 19. Lateral spreading obtained with SRIM in liquid water for various projectiles.

spreading are smaller for the heavier projectiles. Combined with the increased biological efficiency (high RBE and OER close to 1), there is a clear advantage in using the heaviest ions to irradiate malignant tumors. There are nevertheless two limitations in using the heaviest ions.
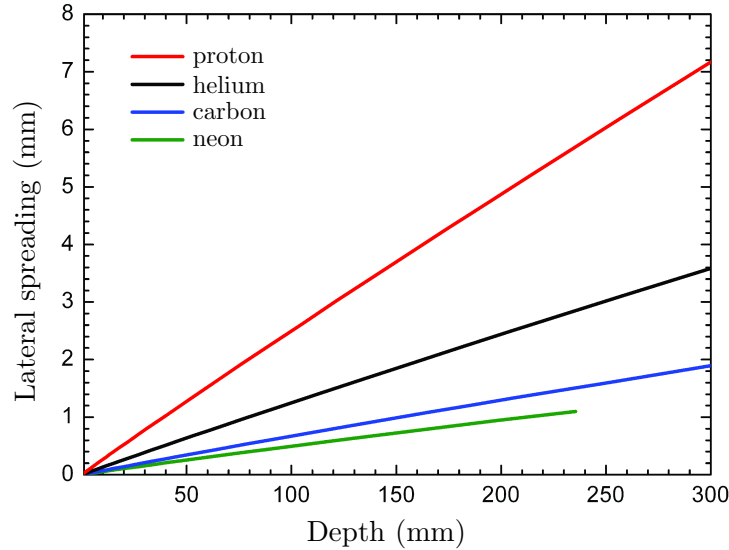
The first one is the maximum energy necessary to reach deep tumors (typically energy corresponding to a 30 cm range in liquid water). This energy increases rapidly with the projectile size. As a consequence, bigger accelerators are needed to reach such ranges which increases a lot the cost and the complexity of the medical accelerator.

The second limitation is due to the nucleus-nucleus collisions which occur in the patient. The effects of the nucleus-nucleus reactions on the dose map are described in details in the next section.

## III. THE ROLE OF NUCLEUS-NUCLEUS COLLISIONS

Nucleus-nucleus collisions play an important role in hadron-therapy. As we will see in this section, the dose map is significantly influenced by this process. The aim of this section is to describe its effects on the dose deposition and what are the main ingredients to an accurate computation of the physical dose map.

The nucleus-nucleus collisions can be schematically described as follows as shown on figure 20. When a projectile hits a target nucleus (panels $a$) and $b$)), light particles are promptly emitted and an excited quasi-projectile and an excited quasi-target are formed (panel $c$)). These excited nuclei decay through consecutive light particle emissions ("evaporation" process) or by a simultaneous break-up ("fragmentation" process). The first step of this description is called the "entrance channel phase" (panels $a$),$b$) and $c$)) and the second step us called the "decay phase" (panels $d$),$e$) and $f$)). For both steps, several models have been developed. A complete nucleus-nucleus collision modeling is achieved by a combination of a model describing the entrance channel and a model describing the decay phase. The influence of the selection of specific combinations of entrance channel and decay model will be seen later.

## A. Influence of nucleus-nucleus collisions on the dose deposition

Nucleus-nucleus collisions have two main effects. The first one is the disappearance of the projectile since the collision will change its nature. As a consequence, this projectile will not deposit its energy up to the Bragg Peak. The second effect is the secondary particle production. These fragments will be often of smaller size but with a velocity close to velocity of the projectile. Because of the $A/Z^2$ scaling of the range for particles with the same velocity, these fragments will deposit their energy at penetration depths beyond the projectile Bragg Peak.

Let us see how those effects manifest. The figure 21 shows the ratio of projectiles which have not experienced a nuclear collision on a nucleus of the absorber with respect to the
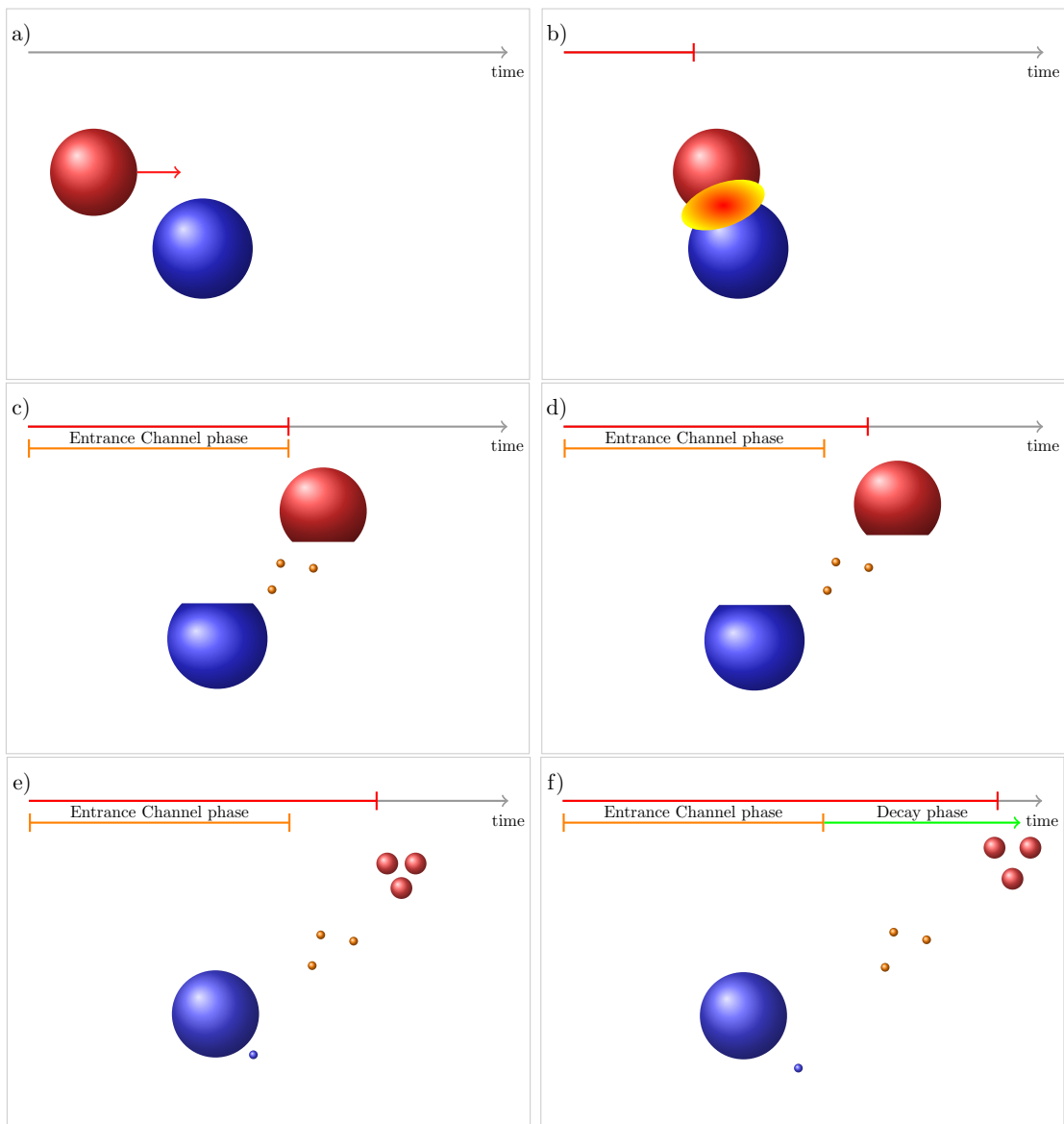


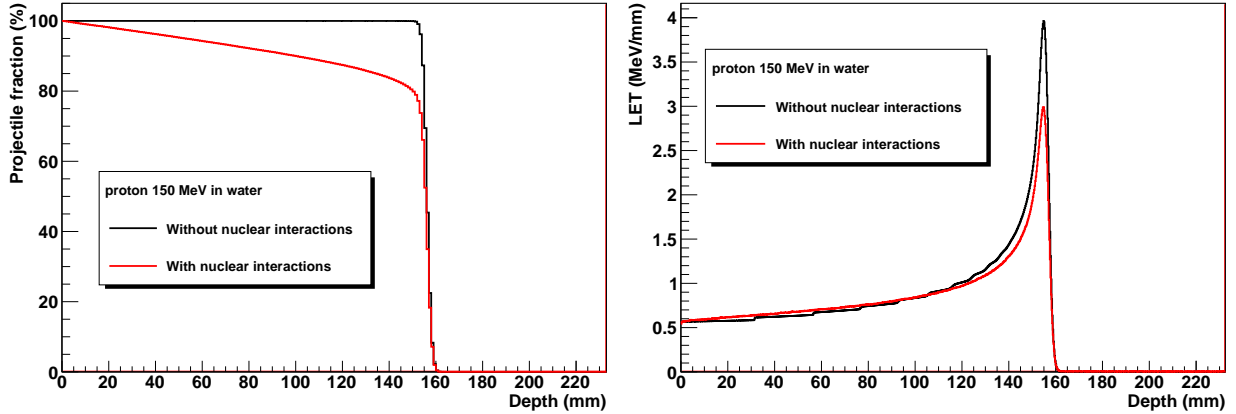Figure 20. Schematic view of a nucleus-nucleus collision

Figure 21. Evolution of the primary protons ratio (left panel) and the mean LET for protons (right panel) with the penetration depth for 150 MeV protons according to GEANT4 simulations.

penetration depth for 150 MeV proton in liquid water (left panel) and the Bragg Curve (the evolution of LET per incident proton with the penetration depth) for 150 MeV protons in liquid water (right panel). This figure results from GEANT4 simulations. On both panels, the black curve corresponds to simulations in which the nucleus-nucleus collision process has been deactivated (label EM) and the red curves to simulations in which the nucleus-nucleus collision process has been activated (label NUC). The effect of the projectile consumption is clearly seen on figure 21. Whereas all projectiles reach the Bragg Peak for EM simulations, only 80% of them reach for NUC simulations. As a consequence, the energy deposition at the Bragg Peak (see left panel of fig 21) is reduced by 20% for NUC collisions compared to EM collisions. Nuclear collisions have no effect on the location of the Bragg Peak which is driven by the Bethe-Bloch equation only. The contribution of secondary fragments, i.e. an energy deposition beyond the Bragg Peak, is not directly seen figure 21. Secondary fragments are issued from the target only. Their velocity is very small and hence their range do not exceed few micro-meters. They deposit their energy close to the collision location. The indirect effect lies in the total amount of energy which has been deposited in the absorber. Since some energy is needed to produce fragments, each time a proton collides on a nucleus, one part of the total energy of the system is exhausted in the particle production. As a result, the integral $\int LET(x)dx$ of the Bragg Curve for NUC simulations is only 97% of the projectile incident energy, whereas this integral is equal to the projectile incident energy for EM simulations.

The influence of the nucleus-nucleus reactions on the dose deposition for $^{12}C$ ions is very similar as it can be observed on figure 22 which has been obtained for 290 MeV/u $^{12}C$ ions using the GEANT4 simulation framework. Only 50% of projectiles reach the Bragg Peak (see left panel of figure 22), leading to a reduction of 50% on the energy deposition per incident $^{12}C$ at the Bragg Peak (right panel of figure 22). The ratio of $^{12}C$ ions which do not experience a nuclear interaction decreases exponentially with respect to the penetration depth. As for protons, the locations of the Bragg Peaks are identical for EM and NUC simulations. The $\int LET(x)dx$ integral is equal to 93% of the incident energy for NUC simulations. The difference compared to protons is the energy deposition tail beyond the Bragg Peak. As for protons, the fragments emitted by the target nucleus have a very short range and deposit their energy close to the collision location. The fragments emitted by the fragmenting projectile have a velocity close to the projectile velocity and hence a longer
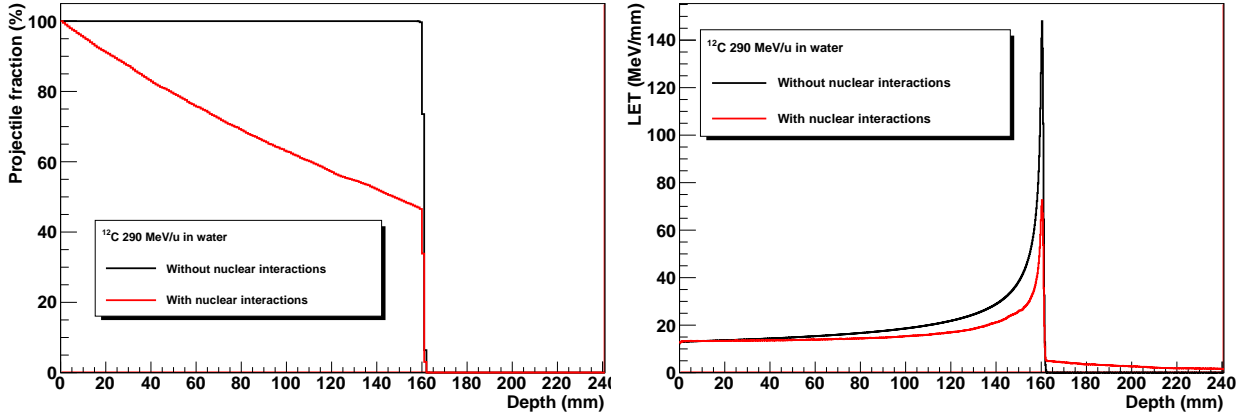
Figure 22. Evolution of the primary $^{12}C$ ions ratio (left panel) and the mean LET for with $^{12}C$ ions (right panel) with the penetration depth.

range. Due to the $A/Z^2$ scaling of the ranges, fragments with a size close to the projectile size (namely Z=3 to Z=6 fragments) will have a range close to the range of the projectile. Lighter fragments will have a much longer range. The tail seen on figure 22, also called the "fragmentation tail", results mainly from the contribution of hydrogen and helium isotopes.

These simulations show clearly that the dose map is significantly changed when the nucleus-nucleus collisions are taken into account.

## B.    Influence of the total reaction cross section

The occurrence of a nucleus-nucleus collision is driven by the total reaction cross section $\sigma_R$. The number $N_{reactions}$ of projectile which experience a nucleus-nucleus reaction when $N$ projectiles in a beam of surface $S$ goes through a thickness $dx$ of material (see figure 23) is:

$$N_{reactions} = N \frac{N_t \, \sigma_R}{S} \qquad (20)$$

where $N_t$ is the number of target nuclei whose expression is;

$$N_t = \frac{\mathcal{N}_a \rho S dx}{M_{mol}} \qquad (21)$$

where $\mathcal{N}_a$ is the Avogadro's number, $\rho$ the material density and $M_{mol}$ the material molar mass. The variation $dN$ of the number of projectiles which remain unchanged after a path on length $dx$ is then:

$$dN = -N_{reaction} = -N \frac{\mathcal{N}_a \rho \sigma_R}{M_{mol}} dx \qquad (22)$$

which leads to

$$N(x) = N_0 \, e^{-x/\lambda} \qquad (23)$$

with

$$\lambda = \frac{M_{mol}}{\mathcal{N}_a \rho \sigma_R} \qquad (24)$$

The exponential decrease of the number of projectiles with the path length is directly driven by the total reaction cross section $\sigma_R$. As an example, let us compute how many
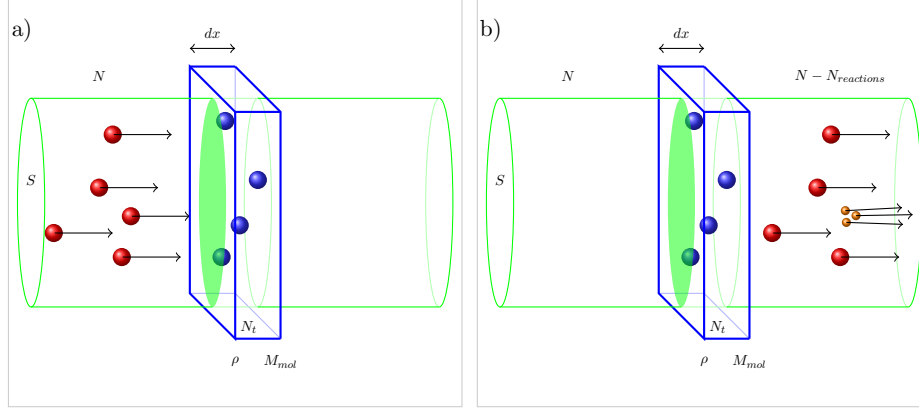
Figure 23. Schematic view of the interaction of a beam of ions crossing a piece of absorber

$^{12}C$ ions at 290 MeV/u reach the Bragg Peak in liquid water. The liquid water density $\rho$ is equal to $1\ mg/cm^3$ and its molar mass is $18\ g/mol$. The Avogadro's number $\mathcal{N}_a$ value is $6.02\ 10^{23} molecules/mol$. The total nuclear reaction cross section $\sigma_R$ of a water molecule is:

$$\sigma_R = 2\sigma_{C,H} + 1\sigma_{C,O} \tag{25}$$

where $\sigma_{C,H} \approx 0.2\,b\ (= 2\,10^{-25}\ cm^2)$ is the total reaction cross section of a carbon ion on a hydrogen nucleus and $\sigma_{C,O} \approx 1\,b\ (= 10^{-24}\ cm^2)$ the total reaction cross section of a carbon ion on an oxygen nucleus. These cross section values are extracted from [Kox87]. The total cross section of a carbon ion on a water molecule is then $\sigma_{C,H_2O} = 2\,\sigma_{C,H} + \sigma_{C,O} \approx 1.4\,b\ (= 1.4 10^{-24}\ cm^2)$. By using all this numerical values, it comes $\lambda \approx \frac{18.}{6.02\,10^{23}\,1.\,1.4\,10^{-24}} \approx 21.35\,cm$. The range of a 290 MeV/u $^{12}C$ ion in water is $x_{BP} = 16\,cm$. Then the number of $^{12}C$ ions that reach the Bragg Peak is $N(x_{BP}) \approx N_0\,e^{-16/21.35} \approx 0.47\,N_0$ with $N_0$ the initial number of projectiles. The value found from this simple expression is very close to the one found in the GEANT4 simulation. One has to notice that it is assumed here that the cross section values do not depend on the projectile's energy which is not true a low incident energies, i.e. for the last few millimeters of the path.

This simple study shows that the average energy deposition per incident ion at the Bragg Peak depends on the chemical composition of the materials crossed by the projectile. This effect is neglected in all TPS's. The dependence of the energy deposition with the $\sigma_R$ value is shown on figure 24. This figure shows the average LET as a function of the penetration depth of $^{12}C$ ions in a stack of materials (skin, cranium, brain white matter, cancerous tumor) obtained with GEANT4. The incident energy distribution has been determined to have a SOBP from 6 cm to 7 cm which corresponds to the tumor size. The corresponding mean LET curve is the black one. Two others simulations have been performed by increasing all the cross section values by 10% (blue LET curve on figure 24) or by decreasing all the cross section values by 10% (red LET curve on figure 24). It is observed that this variation of $\pm 10\%$ on the cross sections values induces a variation of $\pm 3\%$ on the LET value in the tumor. This implies that the reaction cross sections have to be known within 10% to achieve a 3% accuracy on the dose computation. Such uncertainties on experimental cross sections measurements are difficult to reach.
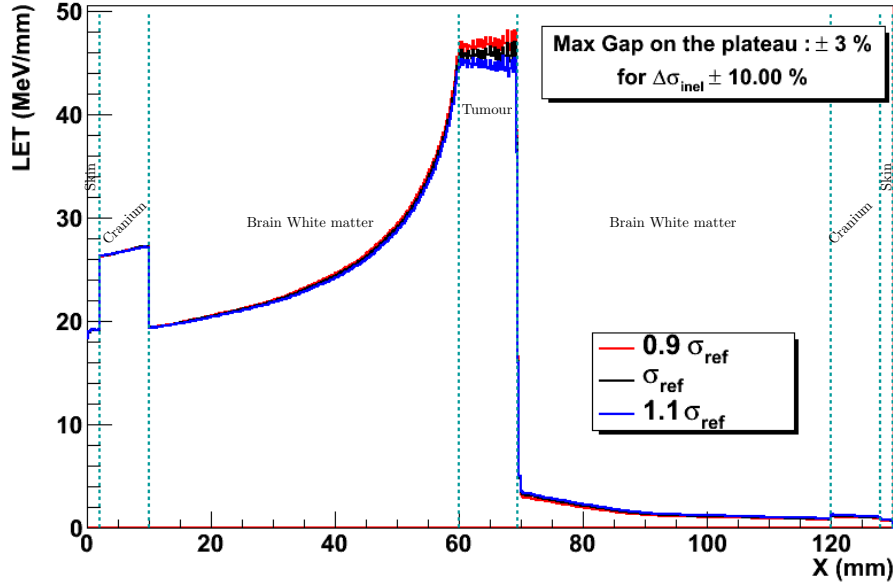
Figure 24. Spread Out Bragg Peak for $^{12}C$ ions crossing a stack of human tissues. Three GEANT4 simulations have been performed with the usual total reaction cross section $\sigma_R$ (black curve), with $0.9 \times \sigma_R$ (red curve) and with $1.1 \times \sigma_R$ (blue curve).

## C.   Contribution of the secondary particles

The contribution of secondary particles is twofold. Firstly, a part of the initial kinetic energy of the projectile is exhausted to produce secondary fragments. When a projectile of mass excess $\Delta m(A_p, Z_p)$ with a kinetic energy $T_p$ hits a target nuclei of mass excess $\Delta m(A_t, Z_t)$ and produces a set of fragments of mass excesses $\{\Delta m(A_i, Z_i)\}$ and kinetic energies $\{T_i\}$, the energy conservation law reads:

$$\Delta m(A_p, Z_p)c^2 + T_p + \Delta m(A_t, Z_t)c^2 = \sum_i \left[ \Delta m(A_i, Z_i)c^2 + T_i \right] \tag{26}$$

by introducing the mass balance $Q = \Delta m(A_p, Z_p)c^2 + \Delta m(A_t, Z_t)c^2 - \sum_i \Delta m(A_i, Z_i)c^2$, the previous equation becomes:

$$\sum_i T_i = T_p + Q \tag{27}$$

For small systems (Z<26) the mass balance $Q$ is negative. As a result, the sum of the kinetic energies of the produced fragments is smaller than the kinetic energy of the projectile. This is why the integral $\int LET(x)dx$ is smaller than the initial kinetic energy of the incident projectile. For example, the kinetic energy reduction of the $^{12}C + ^{16}O \longrightarrow 3\,\alpha + ^{12}C + 2\,p + 2\,n$ reaction is:

$$Q = \Delta m(^{12}C)c^2 + \Delta m(^{16}O)c^2 - 3\,\Delta m(^4 He)c^2 - \Delta m(^{12}C)c^2 - 2\,\Delta m(proton) - 2\,\Delta m(neutron)$$

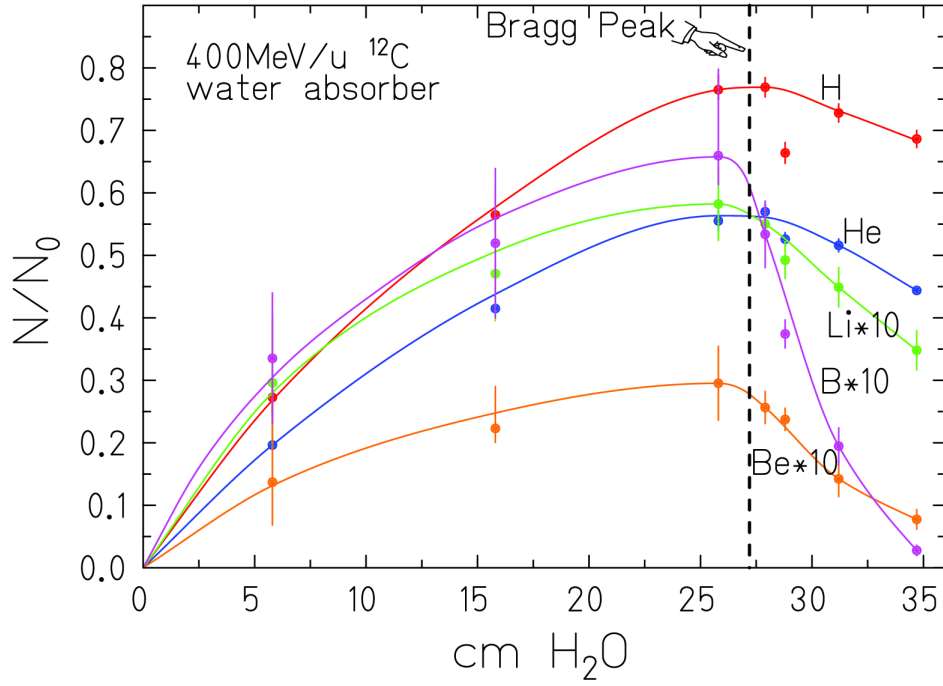$$Q = 0.\,keV - 4737.05\,keV - 3 \times 2424.91\,keV - 0.\,keV - 2 \times 7289.03\,keV - 2 \times 8071.37\,keV$$

Figure 25. Experimental evolution of the mean secondary fragment multiplicities with the penetration depth in liquid water for 400 MeV/u $^{12}C$ ions. Note that the multiplicities of Li, Be and B isotopes have been multiplied by 10 to be visible on the figure. Extracted from [Haet06].

$$Q = -42732.58 \, keV$$

Around $42.7 \, MeV$ are lost due to the nucleus-nucleus collision.

The second type of contribution of secondary particles to the dose map is the energy they will deposit in the target material. As already seen, the particles produced by the quasi-projectile will contribute to the fragmentation tail beyond the Bragg Peak. But since there are produced all along the projectile path, they will also deposit energy behind and at the Bragg Peak. The mean LET at depth $x$ is then the weighted sum of all mean LET's of all particles present at depth $x$:

$$\overline{LET(x)} = \sum_i \nu_{A_i, Z_i}(x) \overline{LET_{A_i, Z_i}(x)} \tag{28}$$

where $\nu_{A_i, Z_i}(x)$ is the multiplicity of fragments with charge number $Z_i$ and mass number $A_i$ at depth $x$ per incident projectile and $\overline{LET_{A_i, Z_i}(x)}$ is their mean LET at depth $x$. The figure 25 shows the evolution of the multiplicity of different fragment type per incident ion with respect to the penetration depth in liquid water for 400 MeV/u $^{12}C$ ions [Haet06]. Behind the Bragg Peak (indicated by the dashed vertical line), the multiplicities of secondary fragments increase with the penetration depth as expected. Beyond the Bragg Peak these multiplicities decrease with the depth. The maximum multiplicities are reached at the Bragg Peak. The measured multiplicity values for hydrogens is $\approx 0.8$ per incident $^{12}C$ and $\approx 0.5$ per incident $^{12}C$ for helium isotopes. At this energy, $\approx 30\%$ of the incident $^{12}C$ ions reach the Bragg Peak. According to the Bethe-Bloch equation the mean LET scales roughly like $Z^2$

for particles having the same velocity. As a consequence, the mean LET value at depth $x$ is dominated by the mean LET of the carbon projectile. The contribution of the hydrogen and helium isotopes to the mean LET remains weak even if their multiplicity is high. The contribution of heavier secondary particles to the mean LET is weak due to their low relative multiplicities. This explains why for the NUC simulations shown on figure 22 the mean LET and the projectile number are reduced by roughly the same factor behind and at the Bragg Peak compared to the EM simulations. Beyond the Bragg Peak, the mean LET is dominated by the contributions of the hydrogen and helium isotopes.
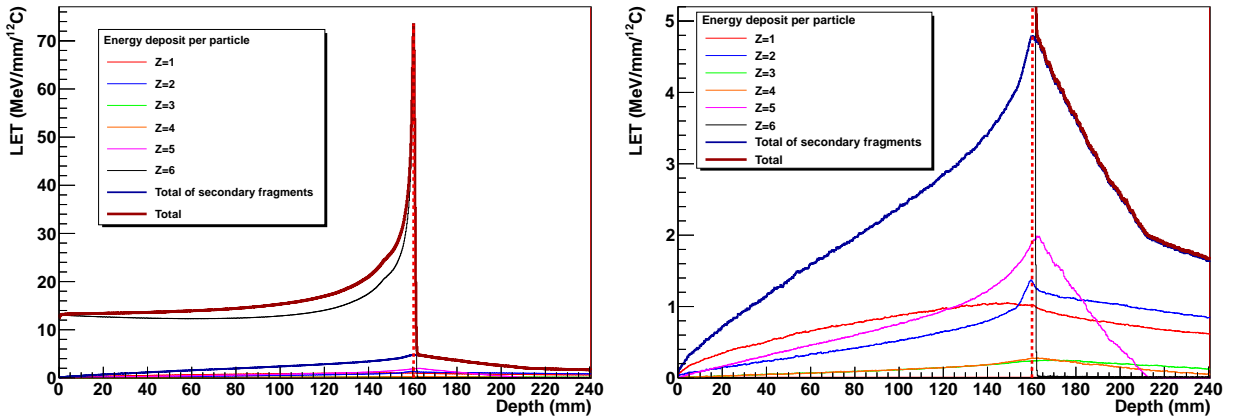


Figure 26. Mean LET value of secondary fragments for $^{12}C$ ions at 290 MeV/u (GEANT4 simulations). The right panel is a zoom on the right panel on low LET values.

An estimation of the contribution of secondary particles to the mean LET value can be seen on the figures 26. The right panel of this figure is a magnification of the figure diplayed on the left panel on low LET values. These figures show the mean LET value of all particles with respect to the penetration depth in liquid water. This has been obtain with the GEANT4 framework for a 290 MeV/u $^{12}C$ ion. The mean LET of secondary fragments increases with the penetration depth and reaches at most $\approx 7\%$ of the mean LET value at the Bragg Peak. Behind the Bragg Peak, the main contributors are the hydrogen, helium and boron isotopes. Beyond the Bragg Peak, the mean LET value results from the contribution of hydrogen and helium isotopes.

This study shows that the energy deposition is strongly affected by the total reaction cross section values. Nevertheless, the specific choice of the nuclear collision model used to describe the nucleus-nucleus collision may have an influence on the computation of the dose. Indeed, the relative multiplicity of secondary particles may change from a model to another and hence modify the evolution of the mean LET with the penetration depth.

## D.   Influence of the nucleus-nucleus collision model on the dose computation

Since the contribution of secondary particles to the mean LET value is around 7% at the Bragg Peak the nucleus-nucleus model may have a non negligible influence on the mean LET value. In order to check this influence, different GEANT4 simulations have been performed using different combinations of entrance channels and decay channels.
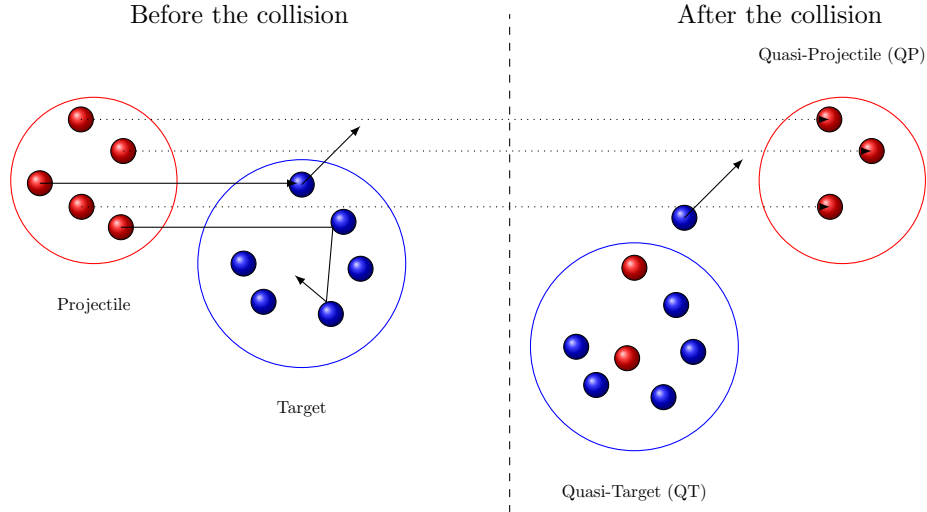
Figure 27. Scheme of the BIC model.

## 1.    Nucleus-nucleus collisions models in GEANT4

The entrance channels used here are the Binary Intra-nuclear Cascade model (label BIC) and the Quantum Molecular Dynamics model (labeled QMD). The BIC model [Cug97, Folg04] assumes that the nucleons of the projectile are free from each other. When a projectile nucleon crosses the target, its trajectory is modified according to the mean field of the target and the interaction cross section of the projectile nucleon on a target nucleon $\sigma_{nn}$. The quasi-projectile is made of projectile nucleons which have crossed the target without interacting with target nucleons. The quasi target is made of target nucleon and of projectile nucleon which have been trapped by at least 2 or 3 successive collisions on target nucleons combined with the interaction of the target mean field. The remaining projectile nucleons (1 collision on a target nucleon) or target nucleons emitted by the nucleon-nucleon emissions are considered as pre-equilibrium particles (see scheme on the figure 27).

The QMD model [Niit95] follows the evolution of the one body density $f(\overrightarrow{r}, \overrightarrow{p}, t)$ with time $t$ according to the Boltzman-Ühling-Ühlenbeck (BUU) equation:

$$\frac{\partial f}{\partial t} + \frac{\overrightarrow{p}}{m}\overrightarrow{\nabla_r}f - \overrightarrow{\nabla_r}U\overrightarrow{\nabla_p}f = I_{collision}(f) \tag{29}$$

The one body function $f(\overrightarrow{r}, \overrightarrow{p}, t)$ is assumed to be the sum of Gaussian functions which are particular solutions of the BUU equation:

$$f(\overrightarrow{r}, \overrightarrow{p}, t) = \sum_i \left[ \lambda_i e^{-\frac{(\overrightarrow{r} - \overrightarrow{r_i})^2}{2\sigma_r^2} - \frac{(\overrightarrow{p} - \overrightarrow{p_i})^2)}{2\sigma_p^2}} \right] \tag{30}$$

In the QMD model, one Gaussian function per nucleon is used. The quasi-projectile, the quasi-target and pre-equilibrium particles are determined by applying a clustering algorithm of the individual Gaussian functions at a well defined time $t_{clust}$.

| Decay Model label | Model for first decay | Model for secondary decay |
|---|---|---|
| EVAP | EVAP | EVAP |
| FBU | FBU if 4 < A < 17 et Z < 9 <br> otherwise EVAP | EVAP |
| MF | MF if A $\geq$ 5 and E*/A $\geq$ 3 MeV <br> otherwise EVAP | EVAP |
| FBUMF | FBU if 4 < A < 17 et Z < 9 <br> MF if A $\geq$ 17 or Z $\geq$ 9 and E*/A $\geq$ 3 MeV <br> otherwise EVAP | EVAP <br> EVAP |
| GEM | GEM | GEM |
| FBUGEM | FBU if 4 < A < 17 et Z < 9 <br> otherwise GEM | GEM |
| MFGEM | MF if A $\geq$ 5 and E*/A $\geq$ 3 MeV <br> otherwise GEM | GEM |
| FBUMFGEM | FBU if 4 < A < 17 et Z < 9 <br> MF if A $\geq$ 17 or Z $\geq$ 9 and E*/A $\geq$ 3 MeV <br> otherwise GEM | GEM <br> GEM |

Table I. Decay models combinations used in GEANT4

The decay models used here are statistical decay models. A weight $\mathcal{W}(E^*, J, \{Z_i, A_i\})$ is computed for each decay configuration $\{Z_i, A_i\}$. The decay configuration is chosen according to its statistical weight $\mathcal{P}(\{Z_i, A_i\}) = \mathcal{W}(E^*, J, \{Z_i, A_i\})/\sum_{configurations} \mathcal{W}(E^*, J, \{Z_j, A_j\})$. Different statistical ensembles (micro-canonical, canonical, grand canonical) or formalisms may be used to compute the configurations weights. The difference between the different models lies in the number of configurations taken into account and the way the statistical weights are computed. We will briefly describe the decay model used for the simulations. For the standard evaporation model (EVAP) [G4Phys, Dost59], the emissions of light particles $(n, p, d, t, ^3He, \alpha)$ only are considered. The weight are computed according to the Weiskopf formalism. The generalized evaporation model is an extension of the EVAP model since all the configurations with two particles are considered. The Fermi Break Up model (FBU) [G4Phys, Fermi50, Kret61, Ephe67] computes the weights for all possible partitions of the fragmenting nucleus. The number of partitions increases very rapidly with the nucleus size and the FBU is limited to $A < 17$ and $Z < 9$ excited nuclei for computational reasons. For heavier nuclei, the statistical Multi Fragmentation model (MF) [G4Phys, Bond95, Botv87] is used. It computes the weights for a sample of partitions randomly chosen among all possible partitions. In GEANT4, the first decay is done through the statistical model chosen. The produced fragments may still be excited. The secondary decays are always done using an evaporation model (EVAP or GEM). They eight combinations used for the GEANT4 simulations of decay models are listed in table I.

By combining the two entrance channel model effect and the eight decay model combinations, 16 simulations have been performed. They have been done for $^{12}C$ ions which energy distribution leads to a Spread Out Bragg Peak (SOBP) ranging from 7.5 cm to 9 cm in liquid water.
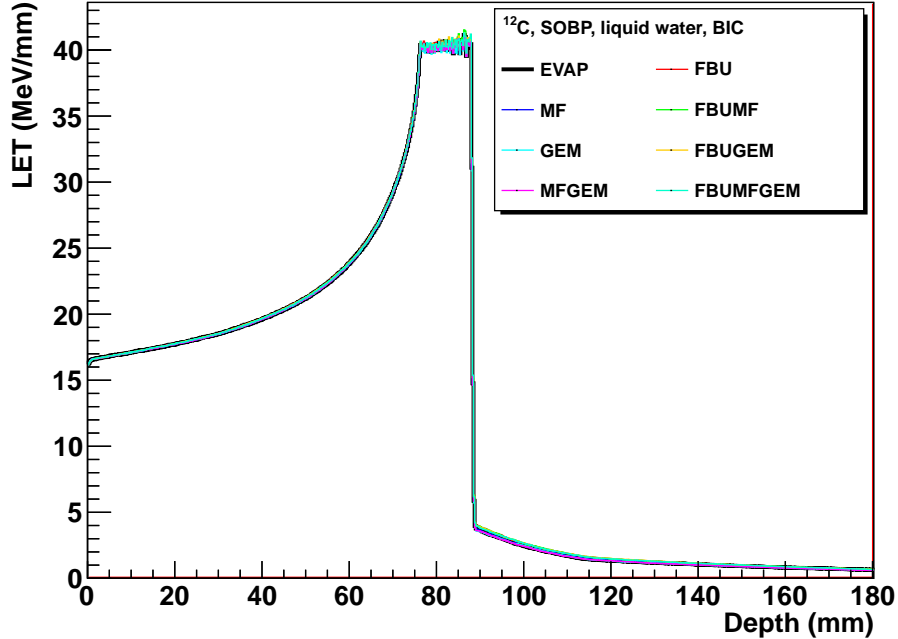
Figure 28. SOBP for GEANT4 simulations using the BIC entrance channel model.

## 2. Simulations results

Let us first check the influence of the decay models on the SOBP by comparing simulations with the same entrance channel model. The figure 28 shows the obtained SOBP when the BIC entrance channel model has been used combined with the eight decay models combinations. The differences on this picture are not clearly seen. In order to better see these differences, we will plot the relative gap $R(x)$ between two mean LET curves, $x$ being the penetration depth:

$$R(x) = \frac{LET_1(x) - LET_2(x)}{LET_1(x)} \times 100 \tag{31}$$

The figure 29 shows the variations of $R(x)$ when the reference SOBP curve is the one obtained by combining the BIC model and the EVAP model. The two horizontal lines on this figure show the 3% limit which is required by the hadron-therapy. The two dashed vertical lines show the SOBP range. We see that before the SOBP, the relative gap between the different curves is very tiny and do not exceed 0.5%. On the SOBP, the relative gaps values are still small and reach at most 1.5%. The biggest differences are observed right beyond the SOBP. The differences can reach up to 15% but the mean LET is small. Since the $^{12}C$ ions are stopped in the SOBP range, only hydrogen and helium isotopes contribute to the mean LET beyond the SOBP. Since their multiplicities depend on the decay model used, big differences are seen when different decay models are used. One sees that the curves are shared in roughly two groups: one group for which the FBU model is used and one group where the FBU model is not used. The MF model has a weak influence. This indicates that most quasi projectiles produced by the BIC model have an excitation energy $E^*/A$ below 3 MeV. The same results are obtained when the QMD model is combined with the eight decay models combinations.

Let us now check the influence of the entrance channel model of the SOBP curve. For
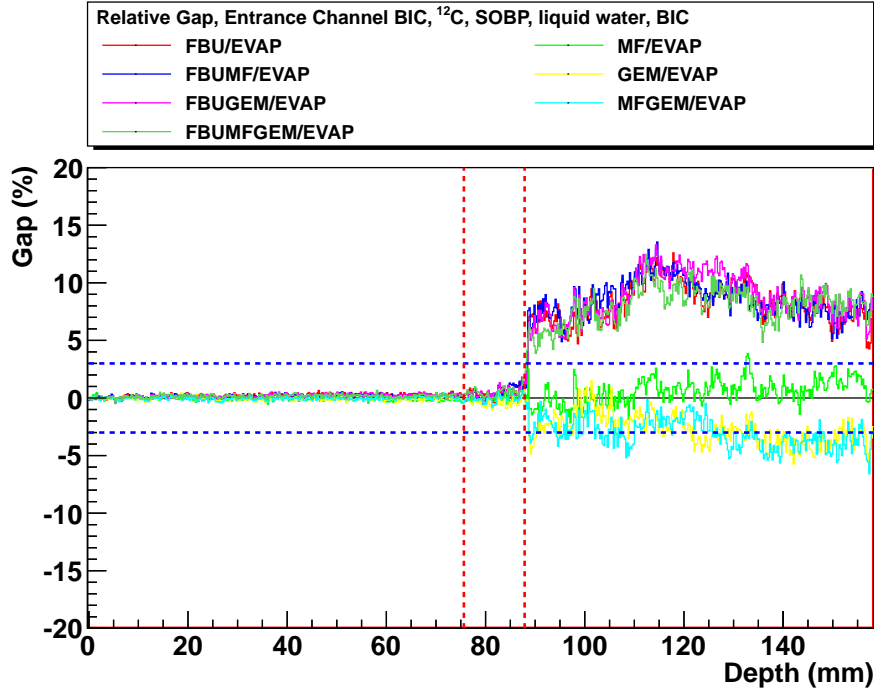
Figure 29. Variations of $R(x)$ for GEANT4 simulations using the BIC entrance channel model.

this, $R(x)$ will be computed by comparing the results of simulations which use the same decay channel combination. The BIC model is used as the reference. The variations of $R(x)$ are shown on the figure 30 for the eight decay model combinations. Behind the SOBP, the relative gap is small and is at most 1.5% just before the SOBP. The $R(x)$ value varies rapidly in the SOBP and reaches 3%. The biggest differences are seen beyond the SOBP and reach 15% since only secondary fragments contribute to the mean LET values at those penetration depths.

### 3.  Conclusions

The variations of $R(x)$ are stronger that the variations observed in the previous study. This shows that the influence of the entrance channel model is bigger than the influence of the decay channel model. Nevertheless, the $R(x)$ values do not exceed the 3% limit in the SOBP. One can conclude that the choice of the nucleus-nucleus model has a weak influence (smaller that 3%) on the computation of the mean LET values. On the contrary, the choice of the nucleus-nucleus model will become essential when secondary particles are used for monitoring purposes. For example, when these secondary fragments are used to control the dose deposition, small uncertainties of their mean multiplicities may induce strong uncertainties on the estimated dose. Additionally this estimated dose will depend strongly on the nucleus-nucleus model chosen to compute it.

### E.  Summary

We have seen in this section that the nucleus-nucleus collisions have a significative influence on the dose map. They do not change the location $x_{BP}$ of the Bragg peak. They reduce
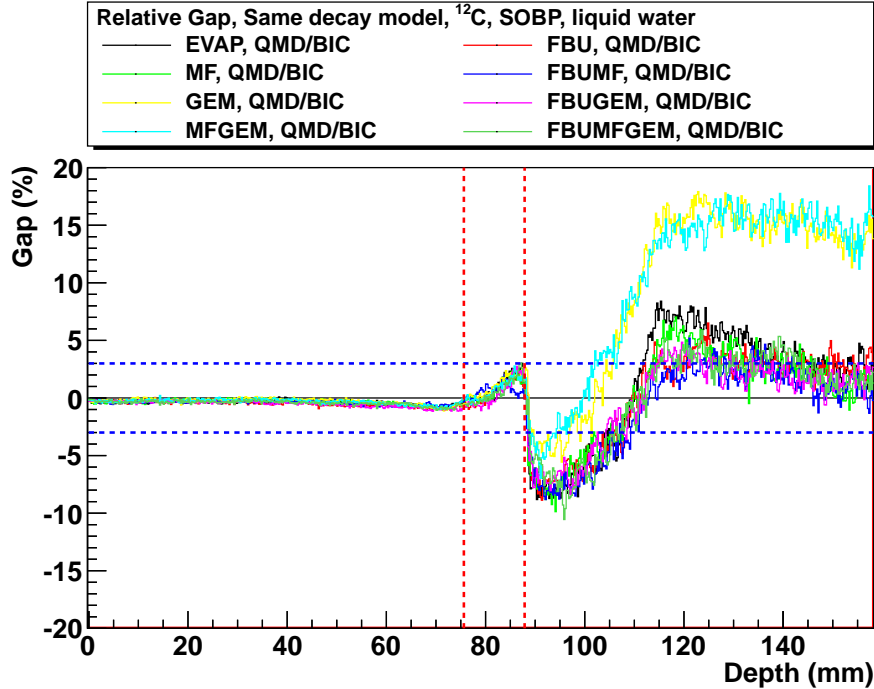
Figure 30. Variations of $R(x)$ for GEANT4 simulations using the same decay channel model.

the number of projectiles all along the path according to an exponential law $N(x) \approx N_0 e^{-x/\lambda}$. Since the number of projectiles is smaller, the energy deposition at the Bragg peak is also reduced according to the same exponential law $LET_{Nuc}(x_{BP}) \approx LET_{EM}(x_{BP})e^{-x_{BP}/\lambda}$. The amplitude of these effects is directly driven by the total nucleus-nucleus reaction cross section $\sigma_R$. The secondary fragments issued from the nucleus-nucleus reactions will deposit their energy beyond the Bragg peak. Since some energy is needed to produce these particles, the total energy deposited in the absorber per incident ion is smaller than its incident energy. The influence of the choice of the nucleus-nucleus collision model on the dose deposition is small ($\leq 3\%$ on the Bragg Peak).

## IV. NUCLEAR PHYSICS METHODS FOR HADRON-THERAPY

The previous part of the lecture has shown that the nuclear physics plays an important role on the dose map. The secondary fragments emitted by the nucleus-nucleus reaction mays also be used to monitor the range or the dose deposition since some of these fragment can come out the body of the patient and can be detected. The charged particle detection can also be used to provide high accuracy imaging devices. These skills can also be useful for designing highly sensitive beam monitors.

This section will present a list of nuclear physics methods that can be useful or adapted to the hadron-therapy.
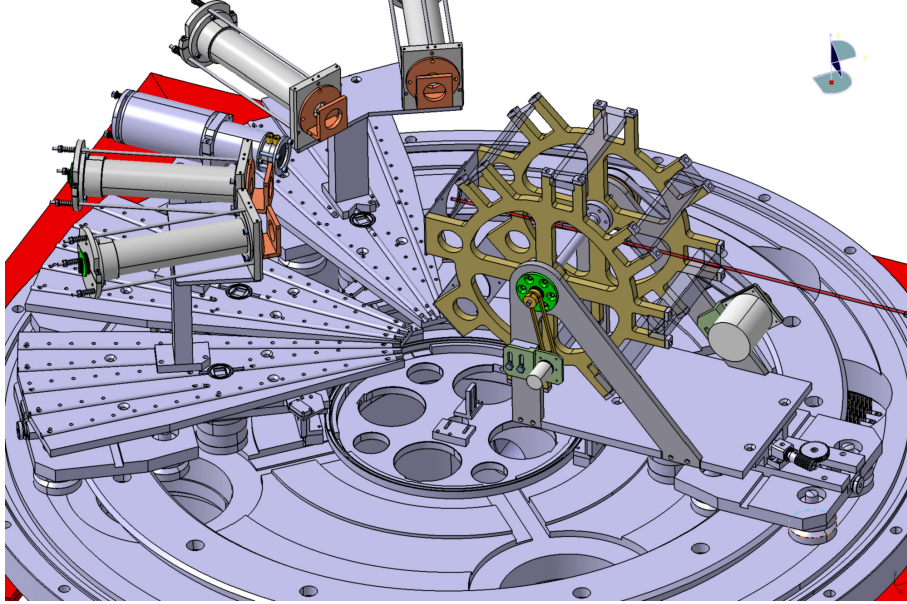
Figure 31. Schematic view of the experimental set-up.

## A. Experimental measurements of the secondary particles production rates

As seen in paragraph III D the nucleus-nucleus models have a weak influence on the mean LET value. But if one wants to use the secondary particles to monitor the dose, the knowledge of the nucleus-nucleus reactions is essential. The models used in the simulations have to be constrained by experimental data.

Many experimental work has already be done by Japanese, German and Italian teams [Mats03, Mats05, Tosh07, Scha96, Gunz04, Gunz08, Haet06]. Most of these experiments where designed to measure the Bragg curve (means LET versus the penetration depth) for $^{12}C$ ions in liquid water. Somme of them were also measuring the mean multiplicity of secondary fragments per incident ion.

Such an experiment has been performed at GANIL in may 2008 [Braunn11]. The $^{12}C$ ions with 95 MeV/u incident energy were thrown to PMMA targets of different thicknesses. The charged particles emitted by nucleus-nucleus reactions were detected with $\Delta E - \Delta E - E$ telescopes. The telescopes were consisting of stacks of Si 300 $\mu m$ thick, Si 1 mm thick and CsI 10 cm thick telescopes. The telescopes were mounted on rotating arms in order to measure the angular distributions of the secondary fragments. The experimental set-up is schematically represented on the figure 31. This experiment has been made in collaboration between the LPC Caen, the IPHC Strasbourg, the IPN Lyon and the CEA/SPhN Saclay laboratories.

The particle identification was achieved by plotting the energy lost in a detector with respect to the energy lost in the preceding detector in the telescope. This is schematically shown on figure 32. Each line seen on the so called "identification maps" correspond to a particle type. A group of thin line corresponds to a defined atomic charge $Z$. Each thin line in a group corresponds to an isotope of charge $Z$.

The detailed description of the experiment and of the experimental identification and calibration methods can be found in the reference [Braunn11].
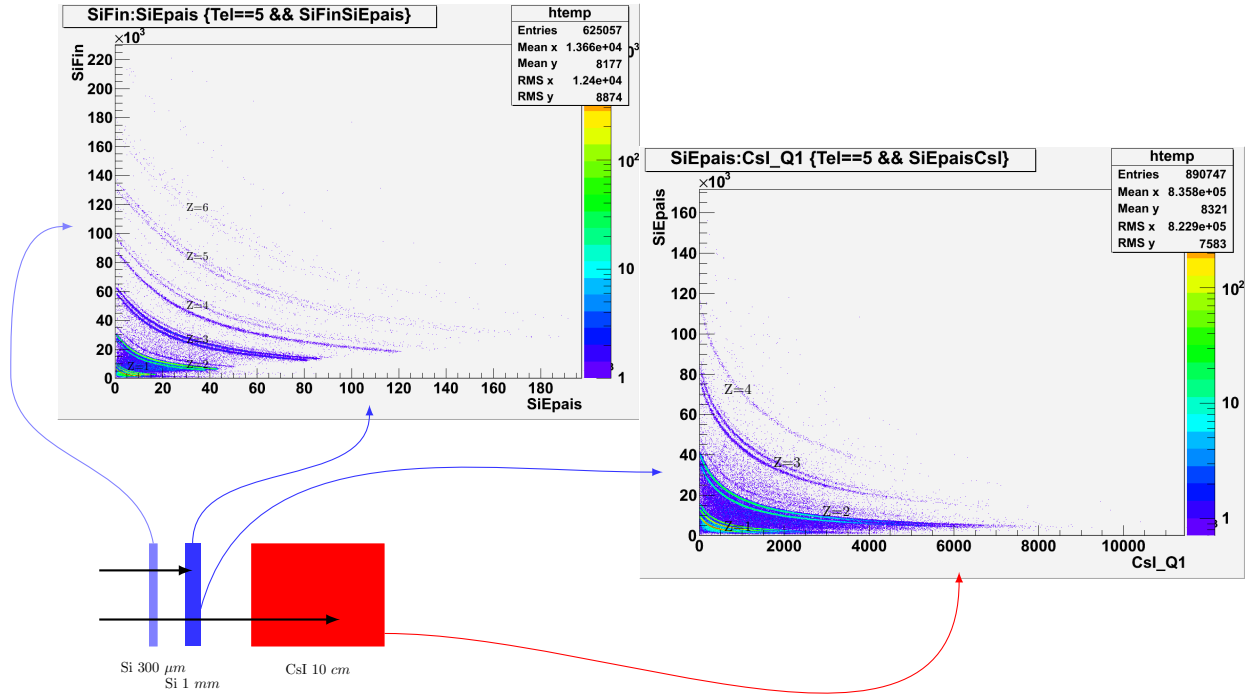
Figure 32. Schematic description of the particle identification.

Once the experimental data have been obtained, one can compare the results of simulations to data. Such a comparison is shown on the figure 33. Simulations have been performed using three different entrance channel models. It is clearly seen that none of the models reproduces the experimental observations at 0°. At 7° the experimental data are barely reproduced. The simulations using the QMD is closer to experimental data than the simulations performed with the two others models.

These studies show that the nucleus-nucleus collisions models are unable to reproduce data with the required accuracy for their use in hadron-therapy. The difficulty with thick targets is that the nucleus-nucleus collision may occur at very different energies. It is then very difficult to select the best models for each individual energy. In order to have a better constraint on nucleus-nucleus collision models, an experiment on thin targets has been performed in may 2011. The beam was the same, i.e. 95 MeV/u $^{12}C$ ions. The experimental set-up was also very similar to the may 2008 experiment. The target used were $C$, $CH_2$, $Al$, $Al_2O_3$, $Ta$ (close to $Ca$) and PMMA $(C_5H_8O_2)$. By combining the results obtained for each target, it will be possible to extract the production rates, the angular and energy distributions of secondary fragments for the $C$, $H$, $O$ and $Ca$ target nuclei. The calibration and the analysis of this experiment is under progress.

## B.   Clinical dose and range control

As already mentioned, the secondary particles with enough energy to cross the patient's body can be detected and used for monitoring purposes. To design such control devices several constraints induced by the standard treatment procedures have to be taken into
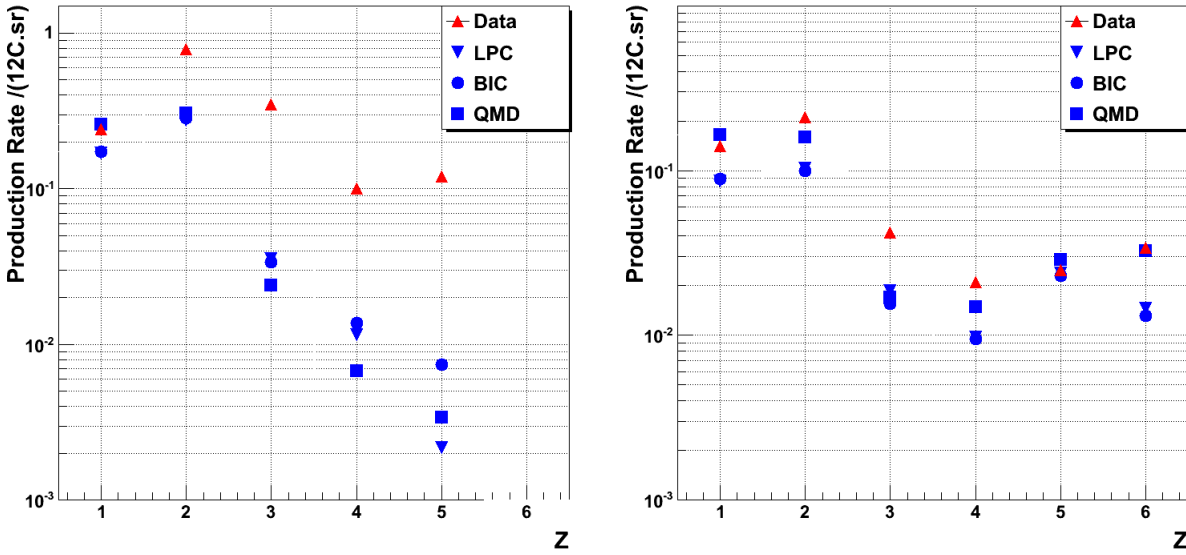
Figure 33. Comparison of GEANT4 simulations (blue symbols) to experimental data (red symbols). The left panel corresponds to the charge production rate obtained at 0° for a 25 mm thick PMMA target. The right panel corresponds to the charge production rate obtained at 7° for a 5 mm thick PMMA target.

account:

- the irradiation lasts 2 minutes at most

- the dose delivered per fraction is 2 Gy

- the total duration of an irradiation fraction is 20 minutes (positioning + irradiation)

To be efficient, a control device has to:

- use a process which produces enough statistics within the 2 Gy constraint

- have detectors with the best possible efficiency

- have a fast electronics and computer processing

- leave enough room for the patient, the positioning control devices, the irradiation table, ...

We will present three different control systems which are under development: the dose and range monitoring by using the $\gamma$ rays coming from the $\beta^+$ emitters formed by nucleus-nucleus collisions; the use of prompt $\gamma$ emissions and the vertex reconstruction of proton emitters.
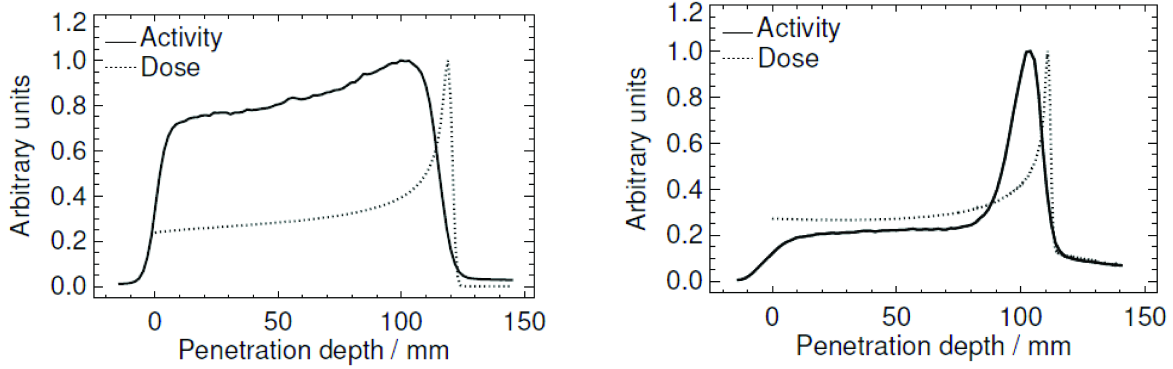
Figure 34. $\beta^+$ emitters activity (black line) and mean LET (dotted line) with respect to the penetration depth in PMMA for 140 MeV protons (right panel) and 259.5 MeV/u $^{12}C$ ions (right panel). Extracted from [Paro04].

### 1. β+ emitters

When the projectile ions hit target nuclei, radioactive nuclei may be formed. Some of them are $\beta^+$ emitters. Using the Positron Emitters Tomography (PET) technique, one can have an image of the path of the ions in the patient [Paro04]. The figure 34 shows variation the $\beta^+$ emitters activity with respect to the penetration depth of 140 MeV protons (left panel) and for 259.5 MeV/u $^{12}C$ ions (right panel) in thick PMMA targets. On each plot, the dotted line corresponds to the Bragg curve of the projectile in the PMMA absorber. The correlation between the $\beta^+$ activity and the Bragg curve is clearly seen. The main $\beta^+$ emitters produced are $^{11}C$ ($T_{1/2} = 20.3\,mn$), $^{10}C$ ($T_{1/2} = 19.3\,s$) and $^{15}O$ ($T_{1/2} = 121.8\,s$). When using $^{12}C$ projectiles, the $^{11}C$ and the $^{10}C$ activities are related to the projectile path in the absorber while the $^{15}O$ activity only result from quasi-target nuclei. This is why a well marked peak is seen close to the Bragg Peak for $^{12}C$ ions. For the protons, the $\beta^+$ activity is only due to quasi-target nuclei.

Such control devices have already been used at the GSI during the medical test period [Paro08]. The control was performed "off-line" and the patient had to stay in place several minutes after the irradiation. The PET camera is seen on 35. The two arms of the camera are set on opposite directions with respect to the patient.

The matching between the planned activity and the measured one is shown on figure 36. The planned dose is shown on the left panel. The planned $\beta^+$ activity is shown in the middle panel and the measured one on the right panel. Since the correspondence of the $\beta^+$ activity and the deposited dose is not accurate enough, this PET imaging has only been used as a range control [Engh04].

Several developments are under progress to improve the performance of this PET imaging. The first improvement consists in doing the $\beta^+$ activity measurement during the irradiation. This requires a fast acquisition electronics and a very good detector efficiency. These technical studies are made at the LPC Clermont-Ferrand laboratory by the AVIRM team [Lest11].

### 2. Prompt γ emissions

Another way to control the dose is to use directly the secondary particles emitted during the nucleus-nucleus collisions. The IPN Lyon team studies the possibility to use the prompt $\gamma$ emissions to monitor the dose and/or the range [Fouhl10, Testa09]. These $\gamma$ have to be energetic enough to cross the patient and to be detected with a good efficiency. The figure

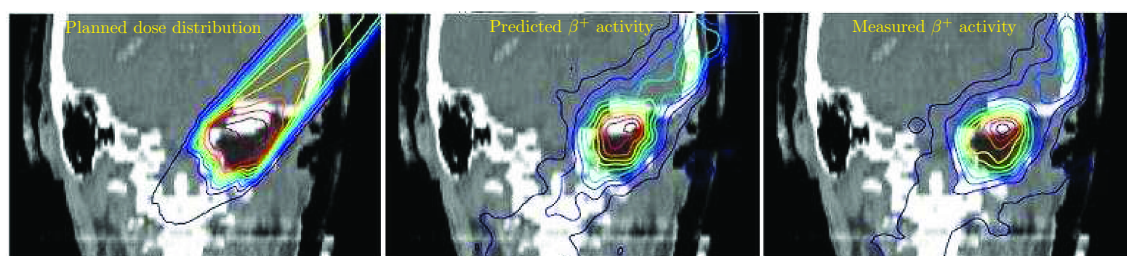Figure 35. Picture of the PET camera used for the range monitoring at the GSI. Extracted from [Paro08]



Figure 36. Example of in-beam PET monitoring showing the irradiation of a skull base tumor at GSI. Left: Planned dose distribution superimposed onto the CT image. Middle: Predicted $\beta^+$-activity distribution calculated from the treatment plan and time course of the irradiation. Right: Measured $\beta^+$-activity distribution. By comparison with the prediction it was verified that the carbon ions were stopped before the brain stem. Extracted from [Engh04]

37 shows the $\gamma$ production rates as a function of the penetration depth targets for 95 MeV/u $^{12}C$ ions (upper panel) crossing a thick PMMA target and for 310 MeV/u $^{12}C$ ions passing through liquid water. On both pictures, the blue curve corresponds to the Bragg curve (mean LET versus the penetration depth). The correlation between the $\gamma$ production rate and the mean LET is clearly seen at 95 MeV/u and barely seen at 310 MeV/u due to a lower statistics. The productions rates are very low ($\approx 5\,10^{-7}$ to $10^{-6}\,\gamma$ per incident $^{12}C$ and per millimeter).

The correlation of the $\gamma$ production rate and the $^{12}C$ Bragg curve is also seen in GEANT4 simulations as shown in figure 38. The discrepancy between the experimental (red symbols) and the simulation (blue symbols) makes questionable the use of prompt $\gamma$ for an accurate dose monitoring. Nevertheless, prompt $\gamma$ emissions may be used for the range monitoring.

In order to measure the $\gamma$ production rates, efficient detectors have to be designed. Two experimental solutions are under evaluation at the IPN Lyon: a collimated $\gamma$ camera and a Compton $\gamma$ camera. A scheme of the collimated $\gamma$ camera is displayed on figure 39. A rank
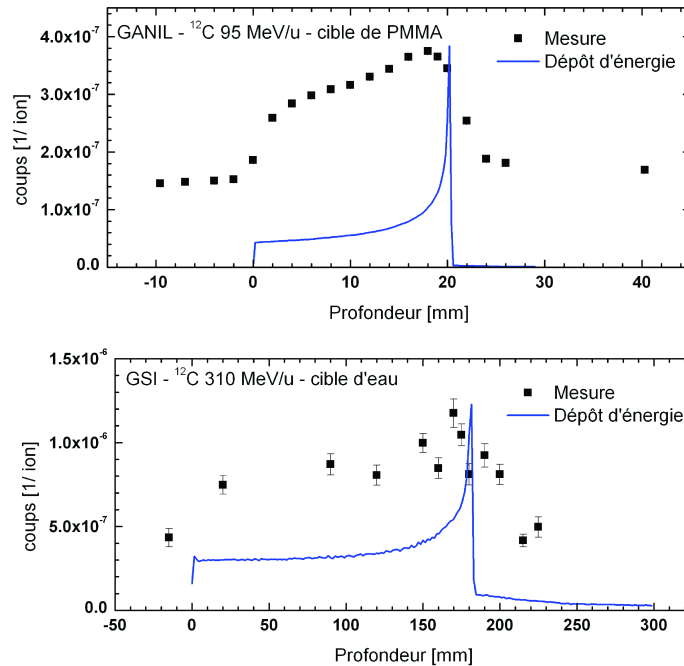
Figure 37. Experimental variations of the $\gamma$ production rates and the penetration depth in the absorber. Extracted from [Fouhl10].
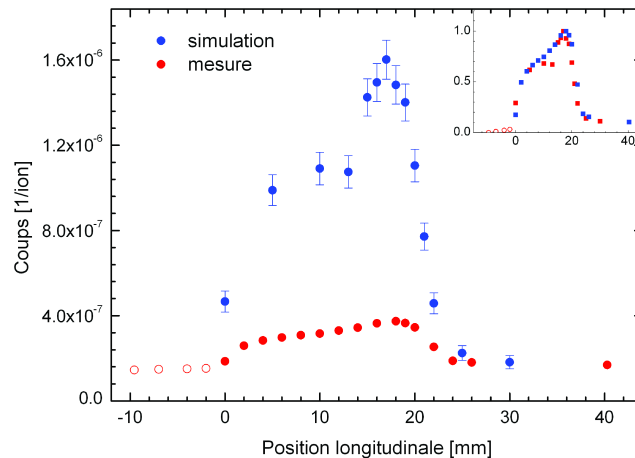


Figure 38. Variations of the $\gamma$ production rates and the penetration depth in the absorber for GEANT4 simulations. Extracted from [Fouhl10].

of collimators select the $\gamma$ emitted in the perpendicular direction with respect to the beam and detected by a rank of detectors. This limits a lot the number of $\gamma$ which can be detected and lowers the efficiency of the control. Another solution would be the Compton $\gamma$ camera (see figure 40). In that case the $\gamma$ crosses two successive position sensitive scatterer. The emission location of the $\gamma$ is achieved by reconstructing its trajectory and by determining the crossing point of this trajectory with the known beam direction. The qualification of these two devices is still under progress.
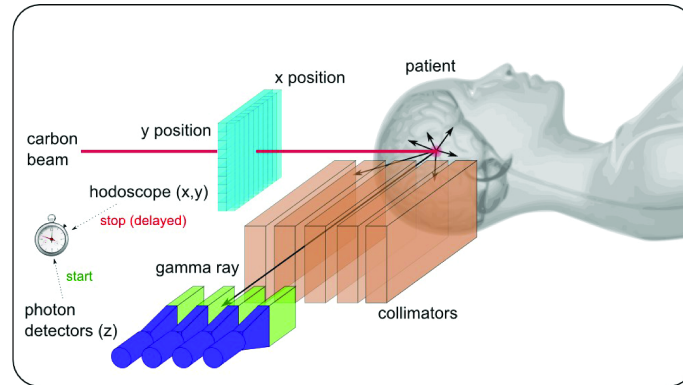
Figure 39. Scheme of the collimated $\gamma$ camera.
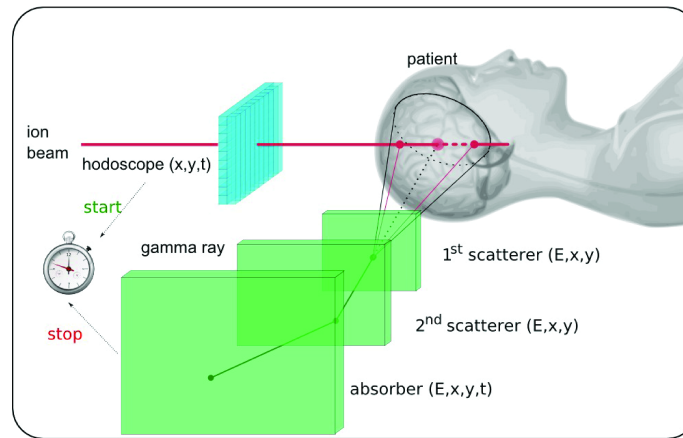


Figure 40. Scheme of the Compton $\gamma$ camera.

## C.  Clinical imaging using protons

The clinical imaging with X-rays is commonly used. The most sophisticated tool is the Computed Tomography (CT) which allows to determine a 3D image of the electronic density from radiographies obtained for different X-rays angular incidences. Many X photons are needed to have an accurate measure of the absorption ratio for each pixel and for each incidence at each angle. A drawback of this technique is that a significant dose (typically few tens of mSv) is deposited in the patient. This may induce unwanted pathologies when too many images are done in a too short period of time.

The Proton Computed Tomography (pCT) has been investigated in order to reduce the nocivity of the imaging while keeping or even improving the accuracy of the 3D electronic density map. This is now possible thanks to the development of compact accelerators and the development of isocentric rotating arms also called "gantries". Instead of measuring an absorption rate, the remaining energy of protons which have crossed a patient is measured at several angles. This requires high energy protons (more than 250 MeV) in order to cross the patient's body. The amount of protons per pixel and per angle is reduced since the mean value of the remaining energy can be determined with a small amount of protons (typically 10 to 100 protons). Since the stopping power of protons is driven by the inelastic collision of protons and electrons, measuring the remaining proton energy gives an access to

the electronic densities of the tissues crossed by the protons. The 3D electronic density map is obtained by using the image reconstruction algorithms commonly used for the standard CT.
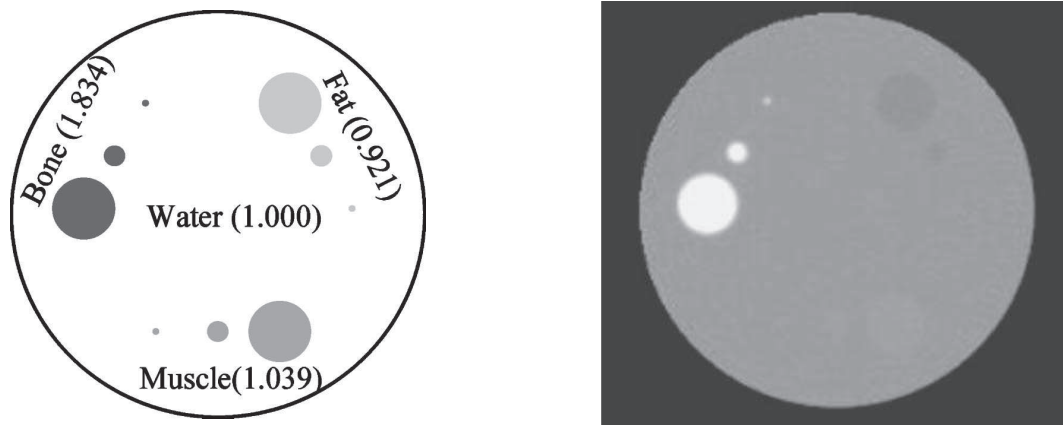


Figure 41. Scheme of the phatom (left panel) and the reconstructed image using pCT (right panel). Extracted from [Schu05].

Such a technique has been tested at the Paul Sherrer Institute (PSI) in Switzerland. They have irradiated a phantom made of materials of known electronic densities and with different sizes [Schu05]. The scheme of the phantom and the reconstructed electronic density map are shown on figure 41. An excellent resolution on the electronic density was achieved with only a $\mu$Sv dose deposition in the phantom center. GEANT4 simulations have also been made and show the same results.

### D. Beam monitors

The main issue for the radio-biology experiments is to determine the actual dose delivered to the cells. Radiological films are most commonly used for this purpose but the dose measurement is not very accurate. Another problem is to have a uniform dose fluency over the whole surface of an irradiation flask. During treatments using ionizing particles, an accurate control of the irradiation is also necessary. Beam monitors are essential tools to control the irradiation process. We will describe shortly the IC2/3 beam monitor which has been developed by the "Medical Applications" team of LPC in Caen in collaboration with the Ion Beam Applications (IBA) company for the proton-therapy centers [Cour11, Cour09].

The use of swept pencil beams is more and more common in proton therapy. It consists in delivering the dose by several spots. Each spot corresponds to a given beam location, a given beam energy and a given beam fluency. The main advantage compared to a passive beam dose delivery which uses beam range shifters and boluses to conform the dose to the tumor geometry is that less matter is set in the beam and hence less secondary particles (mainly neutrons) are produced. The price to pay is that the beam delivery is more complex. The correlations between the beam fluency, the beam energy and the beam location have to be accurately controlled all along the irradiation. An example of an irradiation with swept pencil beams is shown on figure 42. It corresponds to a uniform irradiation of a sphere with a 10 cm radius. The two figures below show the fluency map at two different depths. It can
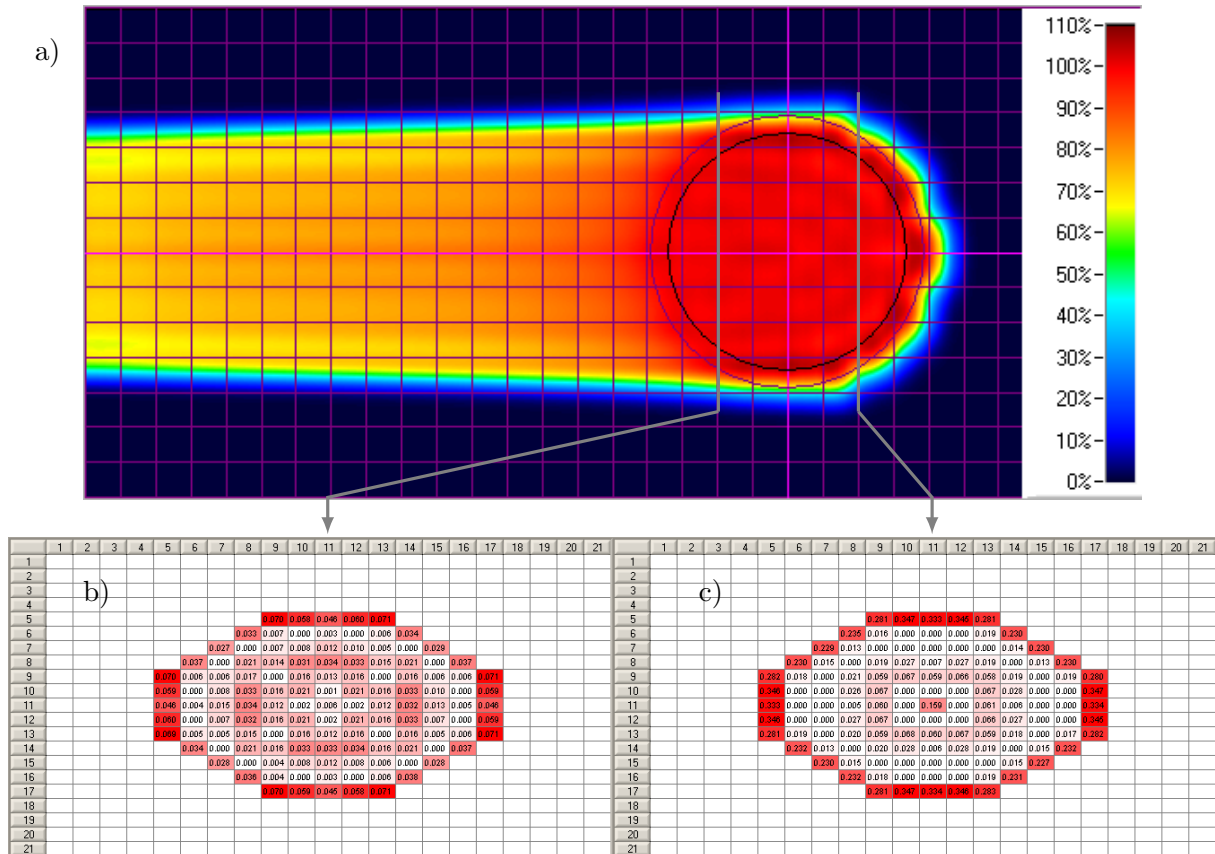
Figure 42. Dose map (a) and resulting fluency maps (b and c) for a proton pencil beam irradiating uniformly a sphere. On each fluency map, the darkest shading corresponds to the highest fluency values. The lowest fluency values correspond to the lightest shadings on the fluency maps.

be seen on these figures that the fluency is maximum on the farthest edges of the sphere and very low at the center and at the nearest edge of the sphere. As a consequence, the device which has to control such fluency maps has to have a wide fluency measurement range and a very precise location measurement. This monitor has to be as transparent as possible in oder to minimize its disturbance on the beam (angular spreading, intensity attenuation).

The IC2/3 beam monitor has been designed and built to control such fluency maps. It consists in a stack of two ionization chambers. The charges are collected by applying a high voltage on the aluminized mylar foils. The gap between the foils is only 5 mm. The resulting water equivalent path of this monitor is 200 $\mu$m. The location of the beam is measured by a horizontal and a vertical set of 64 stripes, each of set being located on one chamber. The fluency is measured every millisecond thanks to a numeric signal processing. The relative measurement of the fluency between the two chambers does not exceed 1%. The beam is located with an accuracy of 70 $\mu$m both horizontally and vertically. A picture of this chamber is shown on figure 43. This monitor is mounted on the nozzles of the treatment rooms at the Westdeutsches Protontherapiezentrum in Essen, Germany. The design of this beam monitor has been done in the framework of cooperation between the LPC Caen and the Ion Beam Application company.
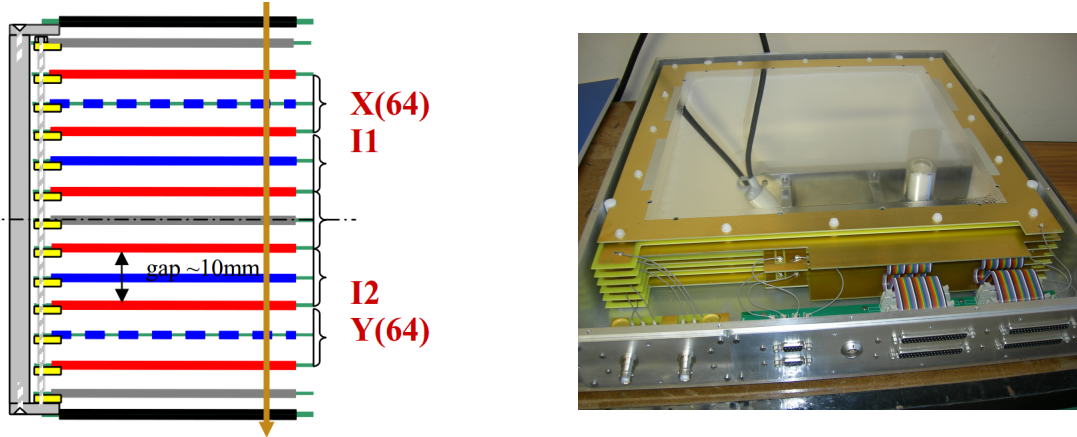
Figure 43. Schematic view and picture of the proton pencil beam monitor developed at the Laboratory of Corpuscular Physics in Caen.

Such monitors are of course needed for the swept carbon beams. The IC2/3 monitor is a good basis to start from.

## V.    CONCLUSIONS AND REMARKS

The use of charge particles for the treatment of cancerous tumors is widely spreading all over the world. This relatively new treatment tool needs to be optimized and improved. Hadron therapy benefits from a good ballistics of heavy ions (Bragg Peak) and their good biological efficiency. It is a very promising means to cure resistant and non operable cancerous tumors and is complementary to other therapies (chemotherapy, surgery, X-ray therapy). It needs heavy infrastructures to work (buildings, accelerators) that increases the cost and the complexity of hadron therapy treatment centres.

The range of a charged particle in the matter is well described by the collisions of ions on electrons (Bethe-Bloch equation) and by the multiple Coulomb scattering process. The nucleus-nucleus collisions do not modify the range of the ions, but modify significantly the dose map. The projectiles consumption and hence the dose at the Bragg Peak are driven by the total reaction cross section $\sigma_R$. Due to the production of secondary fragments, the nuclear reactions induce an energy deposition beyond the Bragg Peak ("fragmentation tail"). The secondary particles may be used to provide new tools to perform in-line dose controls but this requires to select or to build valuable nucleus-nucleus collision models that can reproduce with a very good accuracy the experimental measurements.

Nuclear physicists have an important role to play in optimizing the treatment of cancerous tumors by hadron therapy. They have the technical tools and skills to develop dosimetry devices to control and measure the dose deposited by charge particles in biological materials. They can also help the clinicians by designing high resolution beam monitors and innovative imaging devices. They can also contribute a lot to the improvement of the dose computation by providing valuable models and/or data bases. Nuclear physicists can also help the radiobiologists by building specific dosimetry devices in order to improve the accuracy of their experimental studies and improve the knowledge of the biological effects induced by the

crossing of hadrons in cells.

-------

[Ahlen80] S.P. Ahlen, "Theoretical and experimental aspects of the energy loss of relativistic heavily ionizing particles," Rev. Mod. Phys. 52 1980) 121–173.

[ARCHADE] http://archade.fr/

[Bark63] H.W. Barkas, Nuclear Research Emulsions (Academic, New York), Vol. 1. 1963

[Beth30] H. Bethe, 1930, "Zur theorie des durchgangs schneller korpuskularstrahlen durch materie," Ann. Phys. 397 (1930) 325–400.

[Bich92] Bichsel and Hiraoka, "Energy loss of 70 MeV protons in elements," Nucl. Instrum. Methods Phys. Res. B 66, (1992), 345–351.

[Bich00] Bichsel, H., T. Hiraoka, and K. Omata, Radiat. Res. 153 (2000) 208–219.

[Bloch33a] F. Bloch, "Bremsvermögen von Atomen mit mehreren elektronen," Z. Phys. A: Hadrons Nucl. 81 (1933) 363–376.

[Bloch33b] F. Bloch, "Zur bremsung rasch bewegter teilchen beim durchgang durch materie," Ann. Phys. 408 (1933) 285–320.

[Bragg05] W. Bragg, 1905, "On the $\alpha$-particles of radium and their loss of range in passing through various atoms and molecules," Philos. Mag. 10 (1905) 318–340.

[Bohr40] N. Bohr, "Scattering and stopping of fission fragments," Phys. Rev. 58 (1940) 654–655.

[Bond95] Bondorf J. P., Botvina A. S., Iljinov A. S., Mishustin I. N., Sneppen K., Phys. Rep. 257 (1995) 133.

[Botv87] Botvina A. S. et al., Nucl. Phys. A475 (1987) 663.

[Braunn11] B. Braunn et al., "Nuclear reaction measurements of 95 MeV/u $^{12}C$ interactions on PMMA for hadrontherapy", Nuc. Inst. and Meth. in Phys. Research Section B, Volume 269, Issue 22, (2011), p 2676-2684

[Cour11] C. Courtois PhD thesis, Oct. 2011, Université de Caen Basse Normandie.

[Cour09] Courtois C., Brusasco C., Colin J., De Neuter S., Fontbonne J.M. et al PTCOG 48, Germany (2009) [in2p3-00502502 - version 1]

[Cug97] J.Cugnon, C. Volant and S. Vuillier, Nuc. Phys. A 620 (1997) 475-509

[Dost59] I. Dostrovsky, Z. Fraenkel, G. Friedlander. Phys. Rev. 116 (1959) 683

[Endo96] Endo, M., H. Koyama-ito, S. Minohara, N. Miyahara, H. Tomura, T. Kanai, K. Kawachi, H. Tsuji, and K. Morita, 1996, "HIPLAN-a heavy ion treatment planning system at HIMAC," J. Jpn. Soc. Ther. Radiol. Oncol. 8, 231–238.

[Engh04] Enghardt, W., P. Crespo et al., Nucl. Instrum. Methods Phys. Res. A 525 (2004) 284–288.

[Ephe67] Epherre M., Gradsztajn E., J. Physique 18 (1967) 48.

[ETOILE] http://centre-etoile.org/

[Fano63] Fano U., 1963, *"Penetration of protons, alpha particles, and mesons"*, Annu. Rev. Nucl. Sci. 13, 1–66.

[Fermi50] E. Fermi Prog. Theor. Phys. 5 (1950) 1570.

[FLUKAa] G. Battistoni, S. Muraro, P.R. Sala, F. Cerutti, A. Ferrari, S. Roesler, A. Fassò, J. Ranft, "The FLUKA code: Description and benchmarking", Proceedings of the Hadronic Shower Simulation Workshop 2006, Fermilab 6–8 September 2006, M. Albrow, R. Raja eds., AIP Conference Proceeding 896, 31-49, (2007)

[FLUKAb] A. Ferrari, P.R. Sala, A. Fassò, and J. Ranft, "FLUKA: a multi-particle transport code", CERN-2005-10 (2005), INFN/TC_05/11, SLAC-R-773

[Folg04] G. Folger, V.N. Ivanchenko, and J. P. Wellisch, Eur. Phys. Jour. A 21 (2004) 407-417

[Fouhl10] F. Le Fouhler PhD thesis, 2010, Université Claude Bernard Lyon 1

[Furi00] S. Furihata. Nucl. Instr. and Meth. in Phys. Res. B171 (2000) 251

[GEANT4] S. Agostinelli et al., "Geant4 - A Simulation Toolkit", Nuclear Instruments and Meth-

ods A 506 (2003) 250-303

[G4Phys] `http://geant4.web.cern.ch/geant4/UserDocumentation/UsersGuides/`
`PhysicsReferenceManual/fo/PhysicsReferenceManual.pdf`

[Gunz04] K. Gunzert-Marx, D. Schardt, R.S. Simon, Radiat. Prot. Dosim. 110 (2004) 595– 600.

[Gunz08] K. Gunzert-Marx, H. Iwase, D. Schardt, R.S. Simon, New J. Phys. 10 (2008) 075003.

[Haet06] E. Haettner, H. Iwase, and D. Schardt, "Experimental fragmentation studies with $^{12}C$ therapy beams," Radiat. Prot. Dosim. 122 (2006) 485–487.

[High75] V.L. Highland, "Some practical remarks on multiple scattering," Nucl. Instrum. Methods Phys. Res. 129 (1975) 497–499.

[High79] V.L. Highland, , "Erratum," Nucl. Instrum. Methods Phys. Res. 161, (1979) 171.

[Hir92] Y. Hirao, et al., Nucl. Phys. A538 (1992) 541c-550c

[ICRU51] ICRU report 51: "Quantities and Units in Radiation Protection Dosimetry" (International Commission on Radiation Units and Measurements, Bethesda, MD) 1993.

[ICRU60] ICRU report 60: Fundamental quantities and units for ionizing radiations, 1998.

[Jan82] J. F. Janni (1982) Atomic Data and Nuclear Data Tables, 27, Nos 2–5.

[Kox87] S. Kox, et al., "Trends of total reaction cross sections for heavy ion collisions in the intermediate energy range," Phys. Rev. C 35 (1987) 1678.

[Kret61] M. Kretschmar, Annual Rev. Nucl. Sci. 11 (1961) 1.

[Kuma07] Y. Kumazaki, T. Akagi, T. Yanou, D. Suga, Y. Hishikawa, and T. Teshima, "Determination of the mean excitation energy of water from proton beam ranges," Radiat. Meas. 42 (2007) 1683–1691.

[LEM] Scholz, M., and G. Kraft, 1996, "Track structure and the calculation of biological effects of heavy charged particles," Adv. Space Res. 18, 5–14.

[Lest11] L. Lestang, G. Montarou, N. Pauna, LPC Clermont-Ferrand, France, private communication.

[Mats03] N. Matsufuji, A. Fukumura, M. Komori, T. Kanai, T. Kohno, Phys. Med. Biol. 48 (2003) 1605–1623.

[Mats05] N. Matsufuji, M. Komori, H. Sasaki, K. Akiu, M. Ogawa, A. Fukumura, E. Urakabe, T. Inaniwa, T. Nishio, T. Kohno, T. Kanai, Phys. Med. Biol. 50 (2005) 3393–3403.

[Niit95] K. Niita et al. Phys. Rev. C 52 (1995) 2620-2635

[Paga02] H. Paganetti, A. Niemierko, M. Ancukiewicz, L. E. Gerweck, M. Goitein, J. S. Loeffler, and H. D. Suit, "Relative biological effectiveness (RBE) values for proton beam therapy," Int. J. Radiat. Oncol., Biol., Phys. 53 (2002) 407–421.

[Paro04] K. Parodi Ph.D. thesis (2004) Technische Universität Dresden, Fakultät Mathematik und Naturwissenschaften

[Paro08] K. Parodi et al, Nucl. Instrum. Methods Phys. Res. A 591 (2008) 282–286.

[Paul07] H. Paul, "The mean ionization potential of water, and its connection to the range of energetic carbon ions in water," Nucl. Instrum. Methods Phys. Res. B 255 (2007), 435–437.

[PTCOG11a] `http://ptcog.web.psi.ch/Archive/Patientstatistics-updateMay2011.pdf`

[PTCOG11b] `http://ptcog.web.psi.ch/ptcentres.html`

[PTCOG11c] `http://ptcog.web.psi.ch/newptcentres.html`

[Rossi52] B. Rossi, High-Energy Particles, Prentice-Hall Physics Series (Prentice-Hall, Englewood Cliffs, NJ) 1952.

[Scha96] I. Schall et al., Nucl. Instrum. Methods B 117 (1996) 221–234.

[Schu05] Schulte et al., Med. Phys. 32 (2005) 1035.

[Shardt08] D. Schardt, P. Steidl, M. Krämer, U. Weber, K. Parodi, and S. Brons, 2008, "Precision Bragg-curve measurements for lighton beams in water," GSI-Report 2008-1 (GSI Scientific Report 2007), p. 373 (unpublished).

[Shardt10] D. Shardt, T. Elsässer and D. Schulz-Ertner, Reviews of Modern Physics, Volume 82 (2010) p 383-425.

[SRIM] J. F. Ziegler, J. P. Biersack, and M. D. Ziegler, 2008, SRIM—The Stopping and Range of

Ions in Matter (SRIM, Chester, MD), `http://www.srim.org/`

[Testa09]  E. Testa et al., Nuclear Instruments and Method, vol. 267 (2009) pp. 993-996

[Tosh07]  A. Toshito et al., Phys. Rev. C 75 (2007) 054606.

[TRiP]  M.Krämer et al,Phys. Med. Biol. 45 (2000) 3299–3317.

[Tsai74]  Y.S. Tsai, "Pair production and bremsstrahlung of charged leptons," Rev. Mod. Phys. 46 (1974) 815–851.

[Vasil57]  P.V. Vavilov, "Ionizational losses of high energy heavy particles", Zh. Eksp. Teor. Fiz. 32 (1957) 920–923. [Sov. Phys. JETP 5, 749–751 (1957)].

[Wil46]  "Radiological Use of Fast Protons", R. R. Wilson, Radiology, 47:487-491 (1946)